

COSMOLOGICAL SIMULATIONS OF EARLY BLACK HOLE FORMATION: HALO MERGERS, TIDAL DISRUPTION, AND THE CONDITIONS FOR DIRECT COLLAPSE

SUNMYON CHON¹, SHINGO HIRANO¹, TAKASHI HOSOKAWA^{1,2}, AND NAOKI YOSHIDA^{1,3}

Draft version September 7, 2018

ABSTRACT

Gravitational collapse of a massive primordial gas cloud is thought to be a promising path for the formation of supermassive black holes in the early universe. We study conditions for the so-called direct collapse (DC) black hole formation in a fully cosmological context. We combine a semianalytic model of early galaxy formation with halo merger trees constructed from dark matter N -body simulations. We locate a total of 68 possible DC sites in a volume of $20 h^{-1}$ Mpc on a side. We then perform hydrodynamics simulations for 42 selected halos to study in detail the evolution of the massive clouds within them. We find only two successful cases where the gas clouds rapidly collapse to form stars. In the other cases, gravitational collapse is prevented by the tidal force exerted by a nearby massive halo, which otherwise should serve as a radiation source necessary for DC. Ram pressure stripping disturbs the cloud approaching the source. In many cases, a DC halo and its nearby light source halo merge before the onset of cloud collapse. Only when the DC halo is assembled through major mergers, the gas density increases rapidly to trigger gravitational instability. Based on our cosmological simulations, we conclude that the event rate of DC is an order of magnitude smaller than reported in previous studies, although the absolute rate is still poorly constrained. It is necessary to follow the dynamical evolution of a DC cloud and its nearby halo(s) in order to determine the critical radiation flux for DC.

1. INTRODUCTION

The existence of luminous quasars at $z > 6$ suggests rapid formation and growth of supermassive black holes (SMBHs) in the early universe (e.g., Mortlock et al. 2011; Wu et al. 2015). Theoretically, very efficient mass accretion is needed for the massive BHs to be in place when the age of the Universe was less than 10^9 yr. Even with the maximum Eddington accretion rate, a $100 M_{\odot}$ seed BH can marginally achieve mass growth to $\sim 10^9 M_{\odot}$ by $z \simeq 7$.

The largest mass of the stellar-mass BHs is $20 - 30 M_{\odot}$ in the local universe (Casares & Jonker 2014; Belczynski et al. 2010), but Population III (Pop III) remnant BHs might have larger masses of $\sim 100 M_{\odot}$. In fact, recent theoretical studies suggest that Pop III stars have a broad mass range extending beyond a few hundred solar masses (e.g., Hirano et al. 2014, 2015; Susa et al. 2014). Stellar evolution calculations predict that, with small mass-loss rates, Pop III stars heavier than $300 M_{\odot}$ will leave BHs with essentially the same mass (Heger & Woosley 2002). Although such massive BHs might appear promising SMBH seeds, maintaining the Eddington accretion over nearly 10^9 yr is difficult, if not unphysical, because a variety of radiative feedback effects from stars and accreting BHs reduce the gas accretion rate considerably (e.g., Yoshida 2006; Milosavljević et al. 2009; Park & Ricotti 2011).

The so-called direct collapse (DC) model posits formation of $10^5 - 10^6 M_{\odot}$ supermassive stars (SMSs) in

the early universe. Such a SMS leaves, at the end of its evolution, an equally massive BH (hereafter referred to as DCBH), which can kickstart the rapid mass evolution to SMBHs (e.g., Volonteri 2010; Di Matteo et al. 2012; Valiante et al. 2016). An important question, then, is how often or how rarely DC occurs in the early universe to connect with the observation. The DC model actually assumes multistep processes under a few critical conditions. First, the gas in an atomic-cooling halo collapses nearly isothermally at $T \simeq 8000$ K if the formation of hydrogen molecules is suppressed (Omukai 2001). Three-dimensional simulations show no signatures of vigorous fragmentation in the early collapse stage (e.g., Bromm & Loeb 2003; Inayoshi et al. 2014; Becerra et al. 2015), and thus a single embryo protostar is formed at the cloud's center. The protostar then accretes the surrounding gas at a very large rate of $\dot{M} \sim 0.1 - 1 M_{\odot} \text{ yr}^{-1}$. One can naively expect the well-known relation for a contracting gas cloud, $\dot{M} \sim M_{\text{J}}/t_{\text{ff}} \propto T^{3/2}$, where M_{J} is the Jeans mass and t_{ff} is the free-fall time. Because the temperature $T \simeq 8000$ K is much higher than in the ordinary Pop III formation case with $T \simeq 200 - 1000$ K, the gas mass accretion rate can be large in the DC model. In fact, simulations following the evolution in the late accretion phase demonstrate that such rapid accretion is realized (e.g., Latif et al. 2013). Since the lifetime of a very massive star is typically a few million years, the final stellar mass can reach $\sim 10^5 - 10^6 M_{\odot}$. Hence, this is clearly an appealing model if the above physical processes take place in order.

A variety of models have been proposed to set environments free from H_2 formation and cooling (e.g., Bromm & Loeb 2003; Inayoshi & Omukai 2012; Tanaka et al. 2013). H_2 dissociation by far-ultraviolet (FUV) radiation is one of the major processes. The intensity required for

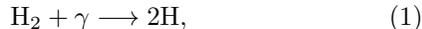
¹Department of Physics, School of Science, University of Tokyo, Bunkyo, Tokyo 113-0033, Japan

²Research Center for the Early Universe, University of Tokyo, Bunkyo, Tokyo 113-0033, Japan

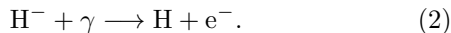
³Kavli Institute for the Physics and Mathematics of the Universe (WPI), Todai Institutes for Advanced Study, University of Tokyo, Kashiwa, Chiba 277-8583, Japan

DC, often denoted by J_{21}^{crit} ,⁴ has been derived by several authors (e.g., Omukai 2001; Shang et al. 2010; Latif et al. 2014; Sugimura et al. 2014; Regan et al. 2014).

There are actually two dissociation processes: one is photodissociation of H_2 molecules (Stecher & Williams 1967),



and the other is photodetachment of H^- , the catalyzer of the H_2 formation via



Reaction (1) is only induced by FUV photons with energy $11.2 \text{ eV} < h\nu < 13.6 \text{ eV}$ in the Lyman-Werner (LW) bands, and reaction (2) has a finite cross section for lower-energy photons with $h\nu > 0.58 \text{ eV}$. Thus, the critical intensity J_{21}^{crit} depends on the exact spectrum of the incident LW radiation, i.e., the nature of the radiation source. For example, detailed 3D simulations of Shang et al. (2010) show that

$$J_{21}^{\text{crit}} = \begin{cases} 10^4 \text{ (for Pop III sources) ,} \\ 100 \text{ (for Pop II sources) ,} \end{cases} \quad (3)$$

where the black body spectra of $T_{\text{eff}} = 10^5 \text{ K}$ and 10^4 K are assumed for the Pop III and II sources, respectively.

Considering necessary conditions for DC such as J_{21}^{crit} , many authors have calculated the cosmological event rate. Dijkstra et al. (2008, 2014) use a Monte Carlo model to count the number of halos irradiated by strong LW radiation exceeding J_{21}^{crit} . In these studies, relevant baryonic physics are implemented in a phenomenological manner to search DC candidates in a large spatial volume ($\sim \text{Gpc}$) considering its parameter dependencies. They study how the baryonic processes, such as how far the metals are dispersed from galaxies, affect the number density of DC. Agarwal et al. (2012) employ a semianalytic model of star and galaxy formation with halo merger trees constructed from cosmological N -body simulations. Johnson et al. (2013) perform cosmological smoothed particle hydrodynamics (SPH) simulations to directly follow the evolution of DC candidate halos and the gas clouds within them. Habouzit et al. (2016) use adaptive mesh refinement simulations to follow hydrodynamical evolution of several DC candidate halos and the gas clouds within them with various feedback models and J_{21}^{crit} . The DC event rate estimates in these studies appear to be very large, in the light of the observed quasar abundance at $z > 6$, a few Gpc^{-3} . More importantly, many of the previous studies do not follow the DC cloud collapse and thus cannot determine robustly whether or not SMSs are formed in the DC halos.

In this paper, we critically examine whether DC is triggered in early dark matter (DM) halos by using direct hydrodynamics simulations. We first locate DC candidate halos in a large cosmological volume by combining a semianalytic model and halo merger trees. We then follow the dynamical evolution of the selected 42 halos to examine explicitly whether the gas clouds collapse gravitationally. We show that the gas density does not increase in most of the candidate halos, largely owing to

strong tidal force caused by nearby massive halos. We find only two successful cases where the collapse is accelerated by halo mergers despite the strong tidal force. The two cases clearly present a viable path for DC in a fully cosmological context. Based on our simulations, we discuss the necessary conditions for DC.

The organization of the paper is as follows. In Section 2, we describe the numerical method. In Section 3, we present the statistical properties of the candidate halos. Section 4 shows that the hydrodynamical evolution of gas clouds in the candidate halos for representative cases. The cloud collapse advances until the density reaches 10^8 cm^{-3} for two cases, which is described in Section 5. We finally discuss implications in Section 6, and give concluding remarks in Section 7.

Throughout this paper, we use the cosmological parameters provided by the Planck Collaboration results (Planck Collaboration et al. 2014), which are $\Omega_{\text{m}} = 0.308$, $\Omega_{\text{b}} = 0.0483$, $\Omega_{\Lambda} = 0.692$, normalized Hubble constant $h = 0.677$, and $\sigma_8 = 0.8288$.

2. METHODOLOGY

We perform a set of multiscale numerical simulations to study the DC model in a realistic cosmological context. We first carry out cosmological N -body simulations to construct halo merger trees. We develop a semianalytic model of star and galaxy formation and implement it for the halo merger trees. In our model, metal enrichment and buildup of LW radiation field are followed in order to locate potential sites for DC. We adopt the conditions for DC that are widely used in the literature (see Section 2.5 below). For about 40 DC sites selected in this manner, we perform zoom-in N -body/SPH simulations to follow the thermal evolution and gravitational collapse of the gas clouds.

2.1. Parent N -body Simulations

We use the parallel Tree-PM code Gadget-2 (Springel 2005) to run our parent cosmological simulation. The initial condition is generated at $z_{\text{ini}} = 99$ by MUSIC (Hahn & Abel 2013), which is based on second-order Lagrangian perturbation theory. The box size is $20 h^{-1} \text{ Mpc}$ on a side. The number of DM particles is 256^3 and the particle mass is $4.08 \times 10^7 h^{-1} M_{\odot}$. The simulation is stopped at $z = 9$. Halos are identified by the friend-of-friend (FOF) algorithm with linking parameter $b = 0.2$.

Zoom-in simulations are performed to study the detailed evolution and structure of the regions that contain potential DC sites. To this end, we first mark 10 most massive halos in our parent simulation, which correspond roughly to $3\text{--}4\sigma$ density peaks. We then regenerate the initial conditions for the zoom-in regions with increasing mass resolution and rerun N -body simulations. The volume of a zoomed-in region is $2.0 (h^{-1} \text{ Mpc})^3$, and the refined particle mass is $1.2 \times 10^3 h^{-1} M_{\odot}$.

In the zoomed-in region, minihalos with $M_{\text{halo}} \sim 10^5 M_{\odot}$, possible Pop III star hosts, are resolved by more than 100 DM particles. This is sufficient to follow Pop III star formation and the associated metal enrichment of the surrounding gas.

2.2. Construction of Merger Tree

We utilize the outputs of the zoom-in simulations to construct halo merger trees. The time interval of the

⁴ J_{21} is the intensity at the Lyman-Werner bands normalized in the units of $10^{-21} \text{ erg s}^{-1} \text{ cm}^{-2} \text{ Hz}^{-1} \text{ str}^{-1}$.

two adjacent outputs is 10 Myr, which is shorter than the dynamical time of collapsing halos at $z < 40$. With the frequently dumped snapshots, we can trace the formation history of Pop III stars.

Merger trees are constructed by tracing the halo member particles. Progenitors and descendants are determined for each halo. A simple particle tracking method often fails because a halo can split into multiple descendants. Therefore, we employ the subhalo-based merger tree algorithm (Springel et al. 2005). Hereafter, we use the term “halo” also for a subhalo.

Subhalos in each FOF halo are defined by SUBFIND (Springel et al. 2005). We trace the subhalo member particles to find a descendent halo(s). This method assigns a unique descendant halo for 99% objects, while the remaining 1% have still multiple descendants. The multiple descendants appear because our time resolution is indeed very short and transient structure of halo mergers can be detected. We simply regard the multiple descendants found in the exceptional cases as a single object.

We use the following five major halo properties: the halo mass M , formation redshift z , the virial temperature T_{vir} , virial radius R_{vir} , and circular velocity V_c , which are defined as follows:

$$T_{\text{vir}} = 1.98 \times 10^4 \left(\frac{\mu}{0.6} \right) \left[\frac{\Omega_m}{\Omega_m(z)} \frac{\Delta_c}{18\pi^2} \right]^{1/3} \left(\frac{M}{10^8 h^{-1} M_\odot} \right)^{2/3} \left(\frac{1+z}{10} \right) \text{ K}, \quad (4)$$

$$R_{\text{vir}} = 0.784 \left[\frac{\Omega_m}{\Omega_m(z)} \frac{\Delta_c}{18\pi^2} \right]^{-1/3} \left(\frac{M}{10^8 h^{-1} M_\odot} \right)^{1/3} \left(\frac{1+z}{10} \right)^{-1} h^{-1} \text{ kpc}, \quad (5)$$

$$V_c = 23.4 \left[\frac{\Omega_m}{\Omega_m(z)} \frac{\Delta_c}{18\pi^2} \right]^{1/6} \left(\frac{M}{10^8 h^{-1} M_\odot} \right)^{1/3} \left(\frac{1+z}{10} \right)^{1/2} \text{ km s}^{-1}, \quad (6)$$

where μ is the mean molecular weight, $\Omega_m(z)$ is the fraction of the energy budget of the matter at z , and Δ_c is the critical overdensity for the halo usually set to be $18\pi^2$ (Barkana & Loeb 2001).

2.3. Semianalytic Model for Star and Galaxy Formation

We employ a semianalytic model of star formation and galaxy formation. We largely follow the method in Agarwal et al. (2012) and briefly describe the implemented processes in the following subsections.

2.3.1. Pop III Star Formation and Metal Enrichment

Pop III star formation is initiated by the onset of H_2 cooling, which becomes efficient in halos with $T_{\text{vir}} \gtrsim 2000$ K (e.g., Tegmark et al. 1997; Yoshida et al. 2003). We assume that a Pop III star forms in a halo when the virial temperature exceeds 2000 K. We adopt a fixed stellar mass of $100 M_\odot$ for the Pop III stars (e.g., Hirano et al. 2015). Our conclusions are not significantly affected by the choice of the Pop III stellar mass (see Section 3.1). The lifetime of a Pop III star is set to be

2 Myr (Schaerer 2002). We assume that all the gas in the host halo is promptly polluted by heavy elements dispersed by a supernova (SN) explosion. Hereafter we refer to the halos before and after the Pop III star formation as “pristine” and “metal-enriched”, respectively.

2.3.2. Pop II Star Formation

After a massive Pop III star dies as an SN, further star formation will be suppressed in the same halo for a while because the gas is evacuated by the energetic SN. When the halo grows sufficiently to attain a mass exceeding a threshold value M_{crit} , continuous Pop II star formation begins. The threshold mass is given essentially by the condition for efficient gas cooling. We fix M_{crit} to be $10^7 h^{-1} M_\odot$ (Loeb & Furlanetto 2013). We label the halos with ongoing Pop II star formation as “star-forming”.

We adopt a three-component model for the baryons; “hot gas”, “cold gas”, and “stars” coexist in a halo. We model the evolution of the baryonic components as follows.

1. Halo growth: When a halo mass increases by ΔM , an accompanying gas of $\Delta M_{\text{gas}} = f_b \Delta M$ is added and it is shock-heated to the halo virial temperature, where $f_b \equiv \Omega_b / \Omega_m$.
2. Cooling: The hot gas component then cools radiatively. We assume that the cooling timescale is approximately given by the local dynamical time $t_{\text{dyn}} \equiv R_{\text{vir}} / V_c$.
3. Star formation: The “cold gas” component is then transformed into stars over the characteristic timescale of $t_{\text{SF}} \equiv 0.1 t_{\text{dyn}} / \alpha$ (e.g., Kauffmann et al. 1993), where α is the star formation efficiency, which is the mass fraction of the cold gas converted into the stars. We set $\alpha = 0.005$.
4. Feedback: An SN explosion returns a part of the cold gas component into hot gas by energy injection. We adopt the mass-converting rate \dot{m}_{reheat} that is proportional to the star formation rate (SFR) \dot{m}_{star} ,

$$\dot{m}_{\text{reheat}} = \gamma \dot{m}_{\text{star}} = \gamma \frac{m_{\text{cold}}}{t_{\text{SF}}}, \quad (7)$$

$$\gamma = \left(\frac{V_c}{V_{\text{out}}} \right)^{-\beta} \quad (8)$$

(Cole et al. 1994). We adopt $\beta = 2.0$ and $V_{\text{out}} = 110 \text{ km s}^{-1}$ in our calculations (Dekel & Silk 1986).

The four processes presented above can be described by the following differential equations:

$$\begin{aligned} \frac{dm_{\text{hot}}}{dt} &= -\frac{m_{\text{hot}}}{t_{\text{dyn}}} + \gamma \frac{m_{\text{cold}}}{t_{\text{SF}}} + f_b \frac{dm_{\text{halo}}}{dt}, \\ \frac{dm_{\text{cold}}}{dt} &= \frac{m_{\text{hot}}}{t_{\text{dyn}}} - (1 + \gamma) \frac{m_{\text{cold}}}{t_{\text{SF}}}, \\ \frac{dm_{\text{star}}}{dt} &= \frac{m_{\text{cold}}}{t_{\text{SF}}}. \end{aligned} \quad (9)$$

We solve these equations explicitly for each time step.

2.4. LW Radiation Field

The formed stars build up UV background radiation, which causes significant impact on early structure formation through H ionization and H₂ dissociation. The intergalactic medium (IGM) is optically thick for ionizing photons before the cosmic reionization, and thus the effects of ionizing photons are relatively limited. We do not consider ionizing photons in our semianalytical calculations, but we examine the effect using one-zone calculations in Section 7.2.

H₂ dissociating photons easily propagate throughout the IGM and affect star formation in other (distant) halos. Photons in the Lyman-Werner bands are emitted from both Pop III and II stars. The stellar luminosities are calculated as follows:

1. Pop III radiation: We use the model spectrum of the 100 M_{\odot} star provided by [Schaerer \(2002\)](#).
2. Pop II radiation: The spectrum of a galaxy is calculated by the population synthesis model STARBURST99 ([Leitherer et al. 1999](#)). We adopt the Kroupa stellar initial mass function (IMF) and metallicity $Z = 0.001 Z_{\odot}$. The total luminosity at the LW bands can be obtained by time-integrating the stellar luminosities over the star formation history,

$$L_{\text{LW},0}(t) = \int_{11.2 \text{ h}^{-1} \text{eV}}^{13.6 \text{ h}^{-1} \text{eV}} L_{\nu,0}(t) d\nu, \quad (10)$$

$$L_{\text{LW,tot}}(t) = \int_0^{t_0} dt' \dot{m}_{\text{star}}(t-t') L_{\text{LW},0}(t'), \quad (11)$$

where $L_{\text{LW},0}(t)$ and $L_{\nu,0}(t)$ are the luminosity and the luminosity differentiated per unit wavelength radiated by the stars formed at time t , respectively, and $L_{\text{LW,tot}}(t)$ is the total luminosity including the contribution of all the stars formed in the past. The reference time t_0 is the time when the Pop II star formation begins.

2.4.1. Pop III Star Formation under the LW Radiation

The condition of the Pop III star formation under LW radiation is investigated by [Machacek et al. \(2001\)](#), who parameterize the criterion for Pop III star formation under the LW radiation as

$$M_{\text{th}} = \psi (1.25 \times 10^5 + 2.8 \times 10^6 J_{21}^{0.47}) M_{\odot}, \quad (12)$$

where M_{th} is the threshold halo mass above which Pop III stars are formed. Note that $\psi \simeq 4$ is a correction factor introduced by [O'Shea & Norman \(2008\)](#). For halos irradiated by nearby radiation sources, we use the criterion of the Pop III star formation $M_{\text{halo}} > M_{\text{th}}$ instead of $T_{\text{vir}} > 2000 \text{ K}$.

2.5. Selection of DC Halos

We impose the following three criteria for DC candidate halos:

1. the halo is chemically pristine;
2. it is irradiated by sufficiently strong LW radiation with $J_{21} > J_{21}^{\text{crit}}$; and
3. it is massive enough for atomic hydrogen cooling to operate, i.e., $T_{\text{vir}} > 8000 \text{ K}$.

The first criterion is required to avoid efficient metal line and dust cooling. The second condition prevents prior Pop III star formation by suppressing H₂ cooling. The last criterion ensures rapid cooling of a massive gas cloud. Here, J_{crit} is set to be 10^4 and 100 for Pop III and Pop II light sources, respectively, as in eq. (3). Note that the assumed spectrum is different from the spectrum calculated by the population synthesis method (Section 2.4). We deliberately made this choice. We give further discussion on J_{crit} in the next section.

Other conditions are also conceivable for DC. For example, the angular momentum of a contracting gas cloud should not be very large to significantly reduce the gas mass accretion rate. Clearly, further direct hydrodynamical simulations following the cloud collapse are necessary to assess additional, if any, conditions. This is indeed the main reason why we perform costly hydrodynamics simulations in the present study.

2.6. Hydrodynamical Simulation

The evolution of the gaseous components in the DC candidate halos is followed using SPH+Tree code Gadget-3 ([Springel 2005](#)). We include 14 primordial species (e⁻, H, H⁺, He, He⁺, He²⁺, H₂, H₂⁺, H⁻, D, D⁺, HD, HD⁺, and D⁻) and follow the chemical and cooling processes, including H₂ photodissociation caused by external LW radiation from nearby light sources. The temporally and spatially varying LW intensity is given by the semianalytic calculations described in Section 2.4. We consider attenuation of the LW intensity by gas self-shielding using the six-ray evaluation scheme ([Yoshida et al. 2003](#)) for H₂ and HD molecules ([Wolcott-Green et al. 2011](#); [Wolcott-Green & Haiman 2011](#)).

The initial DM particle distribution is extracted from the parent N -body simulation (Section 2.1). The gas particles are displaced at the half mesh apart from the DM particle, where the length of one mesh corresponds to the mean separation of the DM particles. The masses of the gas and DM particles are 1.8×10^2 and $1.0 \times 10^3 \text{ h}^{-1} M_{\odot}$, respectively.

We follow the cloud collapse in the DC candidate halos until the halo merges with a nearby metal-enriched halo or until the central gas density reaches 10^8 cm^{-3} . During the cloud collapse, we refine particles so that the local Jeans mass is always larger than 1000 times the particle mass ([Truelove et al. 1997](#)). The practical implementation of our particle splitting is based on [Kitsionas & Whitworth \(2002\)](#). We have confirmed the convergence of our results with using a more strict criterion for the particle splitting, where the Jeans mass is always resolved by more than 10^4 particles.

Occasionally, high-density gas clumps in regions far from a candidate halo cause the simulation time step to be extremely short. To circumvent this difficulty, we harden the equation of state of the gas above threshold densities of $100 - 10^4 \text{ cm}^{-3}$ for nontarget halos. We further reduce the computational cost by employing a ‘‘de-refinement’’ method for nontarget halos, by which the particles are combined to yield low-resolution particles. Again, this procedure dramatically reduces the computational time and enables us to follow a long-term evolution of the candidate halos. We describe further details in Appendix A.

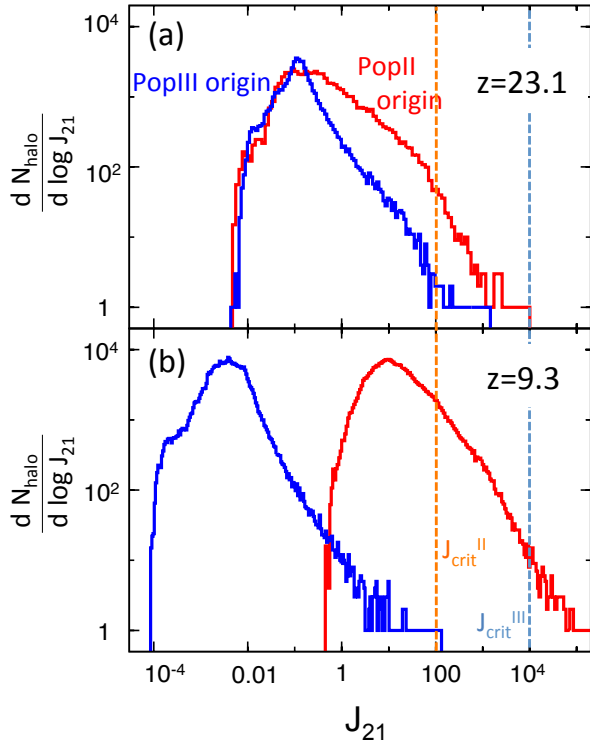


FIG. 1.— Distributions of the LW intensities J_{21}^{III} and J_{21}^{II} at the centers of pristine halos at (a) $z = 23.1$ and (b) $z = 9.3$. The dashed lines show the critical values for Pop II (red) and Pop III sources (blue).

In this study, we use the black-body spectrum with $T_{\text{eff}} = 10^4$ K for the FUV radiation spectrum. Our main goal is to study the collapse of the DC halo starting from the cosmological initial condition and to see the properties of the cosmologically selected DC halos. To investigate the effect of the DC halo selection, we should compare our results with the previous studies on the same conditions except with the proper cosmological settings. Because most of the previous studies employ the $T_{\text{eff}} = 10^4$ K black-body spectrum (Shang et al. 2010; Latif et al. 2014, 2015), we use the same spectrum here, and thus we adopt $J_{\text{crit}} = 100$ for the Pop II light sources in Section 2.5. Note that more realistic spectra of metal-poor galaxies actually provide a higher value of $J_{\text{crit}} \sim 1000$ (Sugimura et al. 2014).

3. RESULTS FROM THE N -BODY SIMULATION

3.1. Star Formation and the LW Radiation

In the zoom-in regions, the first Pop III star is formed at $z \simeq 35$. The background LW radiation intensity J_{21} originating from Pop III stars (J_{21}^{III}) is peaked at $z \simeq 30$ but gradually decreases afterward. Pop II sources first appear at $z \simeq 28$ and J_{21} originating from Pop II sources (J_{21}^{II}) grows rapidly to the global mean of ~ 10 at $z \simeq 10$.

Figure 1 shows the distribution of J_{21} evaluated at the centers of all the pristine halos at (a) $z = 23.1$ and (b) 9.3. Except for the shift of the the peak intensity, the overall distributions appear similar between the two epochs. The distribution scales as $\propto J_{21}^{-1.6}$ for the higher end, and the lower end decreases exponentially. Our result is broadly consistent with that in Agarwal et al. (2012). Interestingly, the slope at the higher end in our

TABLE 1
PROPERTIES OF DC CANDIDATE HALOS

ID	M_{halo} [$10^6 h^{-1} M_{\odot}$]	z	R_{vir} [h^{-1} kpc]	R_{dist} [h^{-1} kpc]	t_{ff} [Myr]
DC0 (S1)	8.37	21.1	0.23	1.27	80
DC1	6.36	19.8	0.22	0.81	28
DC2 (F2)	5.91	19.1	0.22	1.79	50
DC3	6.45	19.1	0.23	1.99	60
DC4	6.47	19.1	0.23	0.99	37
DC5	6.00	18.7	0.23	1.11	50
DC6	7.32	18.4	0.25	2.57	50
DC7	8.05	17.5	0.27	3.93	60
DC8	6.31	17.5	0.25	3.02	35
DC9	6.21	17.3	0.25	4.48	60
DC10	6.88	17.2	0.26	5.24	65
DC11	7.21	17.2	0.27	4.78	120
DC12	7.78	16.9	0.28	2.79	240
DC13	8.12	16.4	0.29	0.39	35
DC14 (F1)	5.71	16.4	0.26	3.10	70
DC15	6.64	16.4	0.27	2.29	85
DC16	18.3	16.4	0.38	0.17	65
DC17	8.69	16.4	0.30	3.45	100
DC18	9.45	16.2	0.31	5.85	70
DC19	7.16	16.0	0.28	4.96	75
DC20	12.3	15.9	0.34	2.42	25
DC21	8.07	15.7	0.30	5.39	70
DC22	7.81	15.7	0.30	6.88	85
DC23	7.53	15.5	0.30	1.94	50
DC24	7.92	15.5	0.30	1.64	40
DC25	7.96	15.5	0.30	4.06	140
DC26	8.46	15.3	0.31	7.36	120
DC27	10.0	15.1	0.34	3.10	65
DC28 (S2)	7.27	14.9	0.31	6.29	105
DC29	7.04	14.7	0.31	4.45	70
DC30	7.31	14.7	0.31	4.26	65
DC31	4.51	14.2	0.27	1.31	110
DC32	7.61	14.2	0.32	5.92	70
DC33	8.78	14.0	0.34	4.00	65
DC34	10.9	14.0	0.37	4.26	100
DC35	8.98	14.0	0.35	4.07	65
DC36	9.63	13.8	0.36	6.08	80
DC37	9.53	13.5	0.37	8.62	100
DC38	9.50	13.0	0.38	5.71	130
DC39	10.1	12.6	0.40	6.17	70
DC40	11.7	11.8	0.44	3.51	65
DC41	11.4	11.1	0.47	6.19	65

Note. Column 1: ID of the DC halo. Column 2: mass of the DC candidate halo. Column 3: the redshift. Column 4: the virial radius. Column 5: the distance from the source halo. Column 6: the time of the infall to the center of the source halo. Column 2-6 are the value when halos meet the DC criteria.

study is smaller than that of the Monte Carlo studies of Dijkstra et al. (2008, 2014); Inayoshi et al. (2015), who employ a two-point correlation function to populate galaxies. The difference is likely caused by the assumed correlation at the small separation of $r \lesssim 1$ kpc. We have checked that the above features remain unchanged also for more massive halos with masses greater than 10^6 and $10^7 M_{\odot}$.

We find that only the Pop II LW field exceeds the critical values for DC. Although a Pop III star is brighter in UV than a Pop II star with the same mass, the global Pop III star formation rate density (SFRD) is overall small. For Pop III sources, moreover, the critical intensity J_{21}^{crit} is higher than for Pop II sources (vertical dashed lines in Fig. 1) because of their higher effective temperatures (equation 3). For these reasons, it is unlikely that the Pop III LW radiation only causes DC events (Agarwal et al. 2012). We thus consider mainly the LW radiation coming from Pop II stars. We note here that J_{21} varies in time and is larger by an order of magnitude than J_{21}^{II} when a DC cloud collapses. This is because the luminous source (galaxy) attracts the DC cloud gravitationally, as we discuss below in Section 4.3.

3.2. DC Candidate Halos

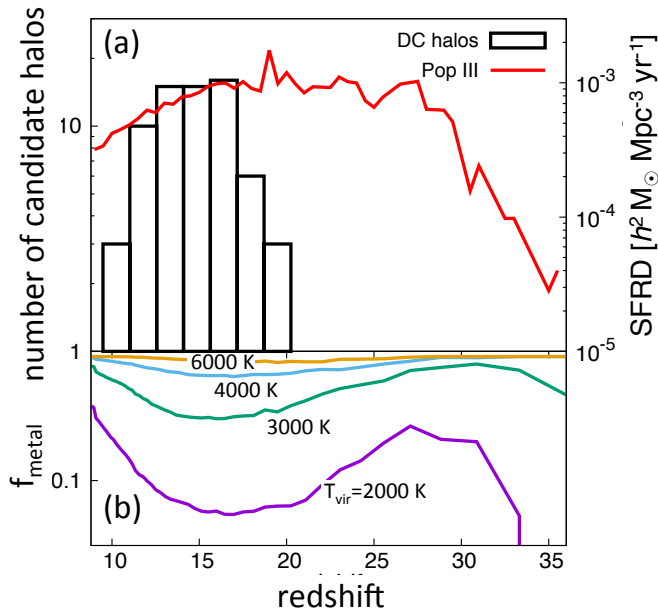


FIG. 2.— (a) Number of DC candidate halos (black) and the Pop III SFRD (red) as functions of redshifts for all the zoomed-in regions. (b) Time evolution of the fraction of metal-enriched halos. Each line corresponds to the fraction for halos with $T_{\text{vir}} = 2000$ (purple), 3000 (green), 4000 (blue), and 6000 K (yellow).

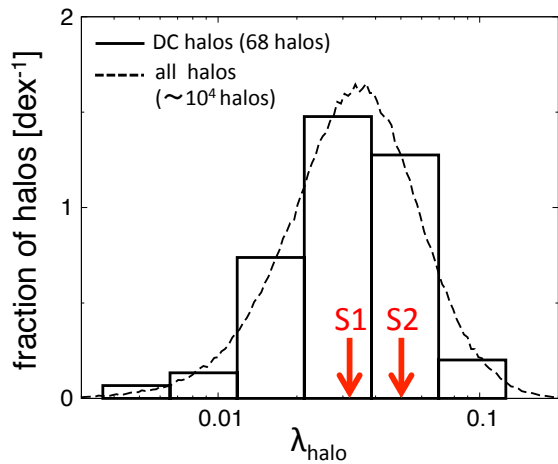


FIG. 3.— Spin parameter distributions for all the halos (dashed) and DC candidate halos (solid). The vertical axis represents the fraction of halos in each bin (dex $^{-1}$). Red arrows show the angular momentum for S1 and S2 halos, which will collapse into the dense core (see Section 4).

In the 10 zoom-in regions, we find 68 DC candidates that satisfy all the three conditions for DC given in Section 2.5. Table 1 summarizes the properties of the 42 halos when each of them meets the DC criteria, whose hydrodynamical evolutions are further followed (Section 4). Detailed evolutions of the halos labeled by F1, F2, S1, and S2 are described in Sections 4.1, 4.2, 4.3, and 4.3.2, respectively. Our hydrodynamics simulations show that only two cases successfully collapse to trigger DC out of the 42 samples. The two cases are dubbed as S1 and S2.

Figure 2(a) shows the redshift distribution of the DC candidate halos and the Pop III SFRD. The number of candidate halos is peaked at $z \simeq 15$ but distributed

widely over $\Delta z \sim 10$, while the Pop III SFRD is almost constant from $z = 30$ to 15. The DC candidate halos appear at lower redshifts than Pop III stars because strong LW radiation sources are needed for DC. After $z = 15$, the formation rate of DC candidate halos and the Pop III SFRD decrease simultaneously, reflecting the fact that the number of newly formed minihalos, the Pop III hosts, decreases after $z = 20$.

A similar trend can be also seen in Figure 2(b), which shows the fraction of metal-enriched halos with $T_{\text{vir}} = 2000, 3000, 4000,$ and 8000 K (purple, green, blue, and yellow, respectively). Around $z = 15$, the fraction of metal-enriched halos starts to increase for all the mass ranges and even for the smallest halos that have $T_{\text{vir}} \simeq 2000$ K. Clearly, after $z = 15$, halos have fewer opportunities to grow up until they attain $T_{\text{vir}} = 8000$ K without being enriched with metals. Metal enrichment causes the numbers of the DC candidate halos and Pop III stars to decrease simultaneously at $z < 15$.

3.3. Spins of DC Candidate Halos

We examine whether the cloud collapse is affected by the spin of its host halo. The degree of halo spin is characterized by the nondimensional spin parameter defined by Bullock et al. (2001):

$$\lambda = \frac{J}{\sqrt{2} M V_c R_{\text{vir}}}, \quad (13)$$

where J is the total angular momentum of the halo. The distributions of the spin parameter for DC candidate halos and of all halos are shown in Figure 3. The spin distribution can be well fitted by a lognormal distribution:

$$p(\lambda) = \frac{1}{\sqrt{2\pi}\sigma_\lambda} \exp\left[-\frac{\log^2(\lambda/\bar{\lambda})}{2\sigma_\lambda^2}\right] \frac{d\lambda}{\lambda}. \quad (14)$$

The best-fit parameters for all halos are $(\bar{\lambda}, \sigma_\lambda) = (0.034, 0.56)$, which is consistent with Bullock et al. (2001) although the halo mass and redshift ranges considered here are very different.

The spin parameter distribution for candidate halos also follows the lognormal distribution with $(\bar{\lambda}, \sigma_\lambda) = (0.043, 0.78)$ and the mean value and the variance of the spin are consistent with those of all the halos.

The red arrows in Figure 3 show the spin parameters of the collapsed DC halos, which host the cloud collapsing into the dense core (see Section 4). The marked values are comparable to the mean value of our detected DC candidate halos and also that of the all the halos in the simulation. This indicates that angular momentum is not a critical factor in the collapse process of DC halos.

4. CLOUD COLLAPSE IN DC CANDIDATE HALOS

We carry out hydrodynamical simulations to follow the subsequent evolution of the gas clouds hosted by selected DC candidate halos. The calculations are performed for 42 halos out of the 68 samples extracted from our parent N -body simulation. We find two “successful” cases, where the gas density at the cloud center reaches

⁵ The absolute value of the Pop III SFRD of our simulation is higher than those found in the previous studies (Agarwal et al. 2012). This is likely owing to the fact that we only focus on the zoomed-in regions, where star formation proceeds earlier.

10^8 cm^{-3} after evolving on an isothermal track with $T \simeq 8000 \text{ K}$. It is highly expected that a massive star, even a supermassive star, is formed in such a gas cloud. For the other cases, however, the clouds do not collapse, often because the host halo merges with a nearby light source halo before the cloud collapses (see Sections 4.1 and 4.2). In this section, we first focus on the evolution of four DC candidate halos, which are listed as F1, F2, S1, and S2 (DC14, DC2, DC0, and DC28 in Table 1, respectively). F1 and F2 are the failed cases, whereas S1 and S2 are successful ones. The overall features of the cloud evolution are summarized in Section 4.4.

4.1. Case F1: Collapse Prevented by Strong Tidal Force

We first study in detail the evolution of a DC candidate halo in which DC does not occur (F1 in Table 1). Figures 4(a) and (b) show the merger history of F1 and the evolution of the LW intensity at the halo center, respectively. LW radiation turns on around $z \simeq 24$ when the halo virial temperature just reaches $T_{\text{vir}} = 2000 \text{ K}$. The intensity increases gradually and reaches the critical value $J_{21}^{\text{crit}} = 100$ at $z \simeq 16.5$. Pop III star formation in the halo is suppressed by the strong LW radiation at $16.5 < z < 24$, when the halo virial temperature is in the range $2000 \text{ K} < T_{\text{vir}} < 8000 \text{ K}$. Note that H_2 cooling would operate otherwise in this temperature range. The halo acquires its mass through smooth accretion and minor mergers, but no major mergers are observed.⁶

The gas density reaches 5 cm^{-3} at $t = 0$ when the halo satisfies the DC criteria (Fig. 4c). However, the gas does not continue contracting, and the density starts to decrease afterward. The halo merges with its nearby light source halo at $t \sim 1.3t_{\text{dyn}}$, before the gas cloud goes gravitational collapse.

The nearby light source halo affects not only the abundance of H_2 in the DC halo by photodissociation, but also the dynamical evolution through tidal forces. The tidal radius of a halo, R_{tid} , outside which the matter will be gravitationally disrupted, is defined by

$$R_{\text{tid}} = \left(\frac{M_{\text{halo}}}{3M_{\text{source}}} \right)^{1/3} d_{\text{dist}}, \quad (15)$$

where M_{halo} is the mass of the candidate halo, M_{source} is the source halo mass that exerts the external gravitational force, and d_{dist} is the distance between the two halos (Binney & Tremaine 1987). In reality, the above expression is modified by a minor factor when the rotation of the candidate halo around the source halo and the density profile of the source halo are taken into account. These complications, however, introduce only a small change less than a factor of 2 for R_{tid} (Binney & Tremaine 1987). We thus use eq. (15) in the following discussion.

Figure 4(d) shows the time evolution of R_{tid} normalized by the virial radius of the candidate halo, R_{vir} . The dashed horizontal line shows where R_{tid} is equal to R_{vir} , that is, the matter at R_{vir} in the DC halo can be stripped by the strong tidal field. After epoch B, when $R_{\text{tid}} \sim R_{\text{vir}}$, the density begins to decrease because the gas cloud is disrupted rather than collapses.

⁶ We define a major merger as one with a mass ratio $m_1/m_2 < 3$, where m_1 is the mass of the larger halo. Otherwise, the merger is defined as a minor merger.

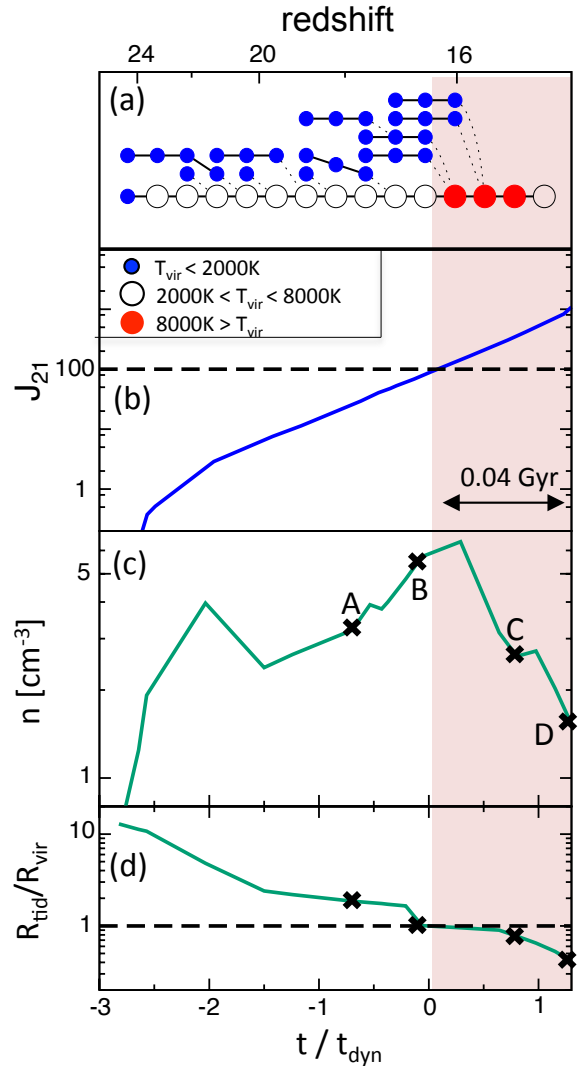


FIG. 4.— (a) Halo merger tree for case F1 (DC14). The small blue filled, black open, and red filled circles represent halos with $T_{\text{vir}} < 2000 \text{ K}$, $2000 \text{ K} < T_{\text{vir}} < 8000 \text{ K}$, and $T_{\text{vir}} > 8000 \text{ K}$, respectively. (b) Evolution of J_{21} at the halo center. The solid line shows the evolution of the LW intensity, and the dashed line indicates the critical LW intensity necessary for the DC criteria, $J_{21}^{\text{crit}} = 100$. (c) Time evolution of the maximum density within the cloud. (d) Tidal radius normalized by the virial radius of the halo. The dashed line indicates where the tidal radius becomes comparable to the virial radius of the host halo. In the shaded region, the virial temperature exceeds 8000 K , with which the atomic H cooling becomes efficient. Points A, B, C, and D are the reference points used in Figure 5. The redshifts corresponding to t/t_{dyn} are shown at the top of panel (a). The reference dynamical time at $t = 0$ is 37.7 Myr . In panel (b), the black arrow represents the physical timescale of 0.04 Gyr .

In Figure 5, the panels in each row show the snapshots at the epochs A–D indicated in Figure 4(a). The panels in the left column show that the temperature of the central part of the cloud reaches 10^4 K at epoch B. The snapshots C and D show that most of the gas has a temperature around 10^4 K . The panel sequence shows that the candidate halo indicated by the square is attracted by the light source halo through epochs A–D. At D, the candidate halo is completely merged with the source halo, together with its surrounding matter. The right panel (D) also shows that the candidate halo and

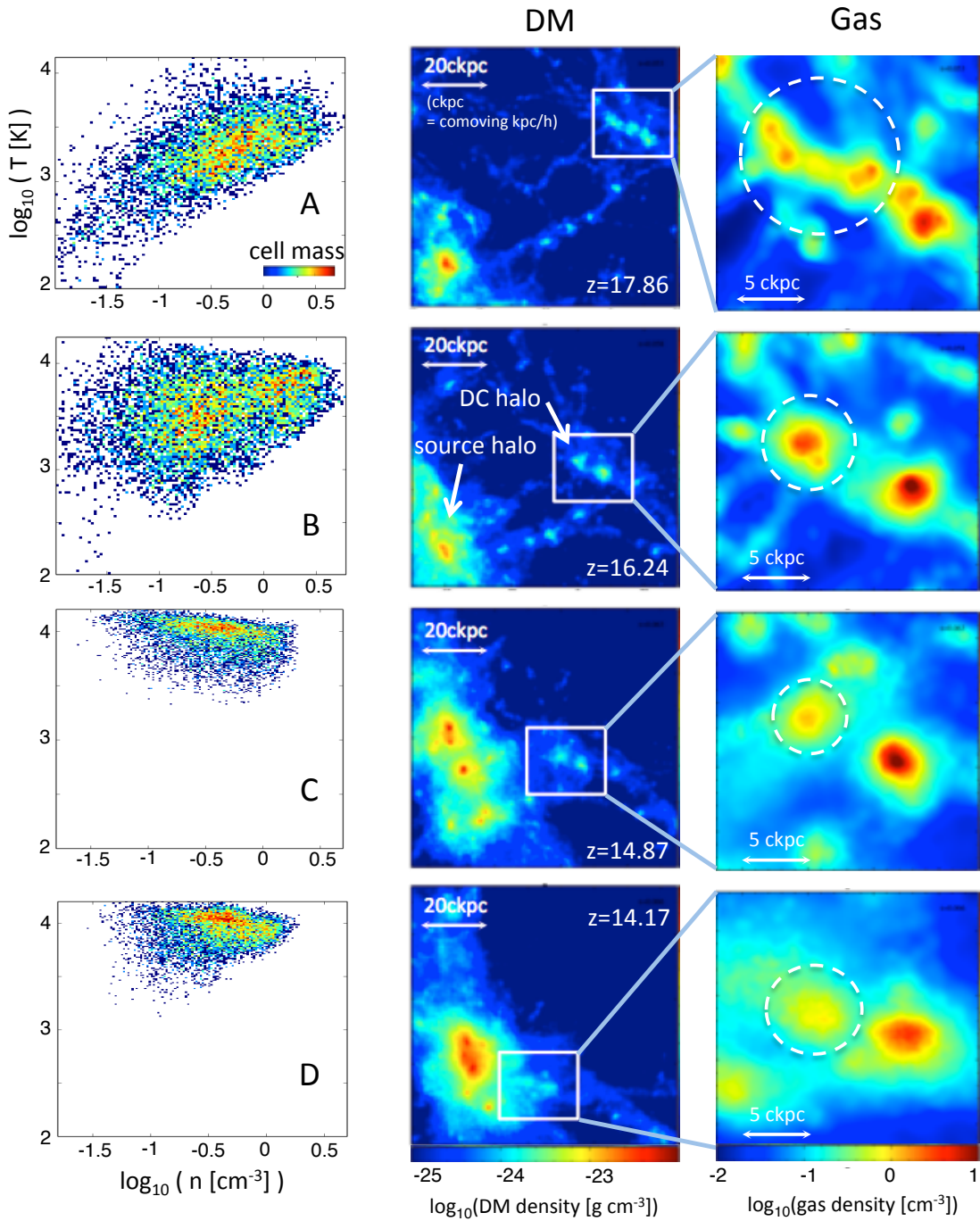


FIG. 5.— Time evolution of the F1 halo at four reference points shown in Figure 4. Left: the scatter plots of the temperature vs. the gas density. The color scale shows the cell mass in each bin. Middle: the projected DM density distribution around the F1 halo. The large clump at the bottom left corner in each panel is the source halo. The candidate halo is inside the white box. The color scale represents the DM density. Right: the projected gas density distributions around the halo. The color scale represents the gas density. There are two main clumps in each panel, and the clump on the left is the DC candidate halo, which is contained by the white dashed circle. The other clump is a halo in which a Pop III star is already formed. In each panel, the comoving length scales of 20 kpc/h and 5 kpc/h are represented with the white arrows.

the gas cloud itself become elliptical in shape and elongated toward the source halo. This is a characteristic feature of tidal disruption, stretching an object toward the external gravitational source. Clearly, the density decrease is caused by the tidal field of the massive light source halo.

The candidate halo experiences multiple mergers with less massive halos after the virial temperature reaches 8000 K (Fig. 4a). The infalling halos carry energy into the center of the candidate halo if they survive to reach the center, in a similar manner to dynamical disk heating (Toth & Ostriker 1992). Once the energy is deposited to the center of the candidate halo, the center starts to expand and the density decreases. Then the cloud becomes more susceptible to tidal disruption. The expanded core is only loosely bounded gravitationally, and the gas density decreases further (Fig. 5 B). Interestingly, this is a two-step process; minor mergers under the strong tidal field initiate the destruction of the cloud. The density decrease at $z \simeq 22$ ($t \sim -2t_{\text{dyn}}$) is caused by a minor merger.

As we will discuss in Sections 4.3 and 6.2, major mergers can help induce gravitational instability at the cloud center. The difference from the above discussion is simply whether or not the merger assembles and brings enough mass toward the cloud center.

4.2. Case F2: Collapse Prevented by Ram Pressure Stripping

We also find that ram pressure often prevents cloud collapse. Figures 6(a) and (b) show the evolution of the density and the tidal radius, respectively. Even after the virial temperature of the halo exceeds 8000 K at $t = 0$, the density decreases continuously. The tidal force of the light source halo becomes comparable to the gravitational force at $t \sim t_{\text{dyn}}$. The halo experiences neither minor nor major mergers for $\simeq 50$ Myr after the halo satisfies the DC criteria.

We suspect that hydrodynamic effects cause the gas cloud to disperse. Ram pressure is given by the product of density ρ_{gas} and velocity v as

$$P_{\text{ram}} \equiv \rho_{\text{gas}} v^2. \quad (16)$$

If a cloud is moving in a dense medium, ram pressure acts on the cloud to strip the outer gas against its self-gravity. The condition for the stripping is given by

$$P_{\text{ram}} > \alpha \frac{GM(R)\rho_{\text{gas}}}{R} \quad (17)$$

(Gunn & Gott 1972; Gisler 1976), where R is the size of the cloud, $M(R)$ is the gravitating mass within R including DM, and α is an order unity parameter that is characterized by the geometry of the cloud. According to the detailed simulations by McCarthy et al. (2008), $\alpha = 2$ is appropriate for a spherical cloud. We find that the ram pressure acting on the cloud is comparable to the gravitational force at $t \sim 0.6t_{\text{dyn}}$ (Fig. 6c).

The discrepancy between the DM and gas profiles exhibits another evidence for the ram pressure stripping acting on the cloud. Figure 7 shows the projected density distributions for DM and baryons at the reference points A, B, C, and D in Figure 6(c). The cloud is moving toward the dense filament at the bottom. On its

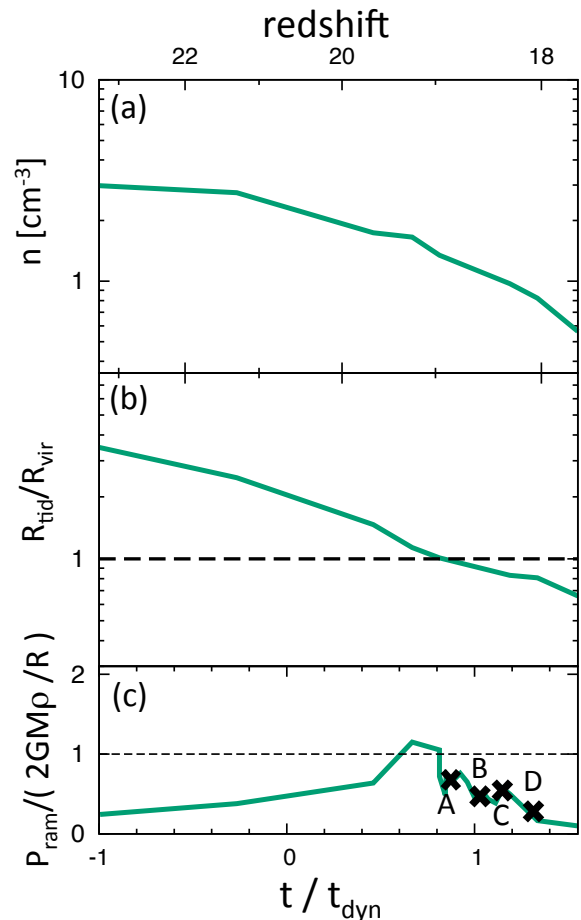


FIG. 6.— (a) Evolution of the gas density in the DC cloud for case F2 (DC2). The horizontal axis represents the elapsed time since the host halo satisfies DC criteria and normalized by the dynamical time at $t = 0$. (b) Evolution of the tidal radius normalized by the virial radius of the host halo. The dashed line indicates where the tidal radius becomes equal to the virial radius of the host halo. (c) Ratio of the ram pressure exerted on the cloud (eq. 16) and the gravitational force per unit area. The dashed line represents where the ram pressure and the gravitational force balance. The points A, B, C, and D are the reference points used in Figure 7. The reference dynamical time at $t = 0$ is $t_{\text{dyn}} = 27.7$ Myr.

way, the cloud is dissolved into the surroundings, while the DM structure remains intact. Clearly, the candidate halo does not experience mergers. Figure 8 shows the density profiles of the (a) DM and (b) gas. The gas density decreases with time, while the DM profile remains almost unaffected.

4.3. Cases S1 and S2: DC Clouds

In cases S1 and S2, the gas cloud continues to collapse and an SMS is likely to form. We mainly discuss the evolution for case S1 below, while the S2 case is briefly discussed in Section 4.3.2 because its overall evolution is quite similar to that of S1.

4.3.1. The evolution of S1

The merger history of halo S1 and the evolution of the LW intensity at its progenitor center are shown in Figures 9(a) and (b). There are two main tree branches (A and B), which are finally merged into the candidate halo. Progenitors in each branch are exposed to strong radiation with nearly the same LW intensity, which suppresses

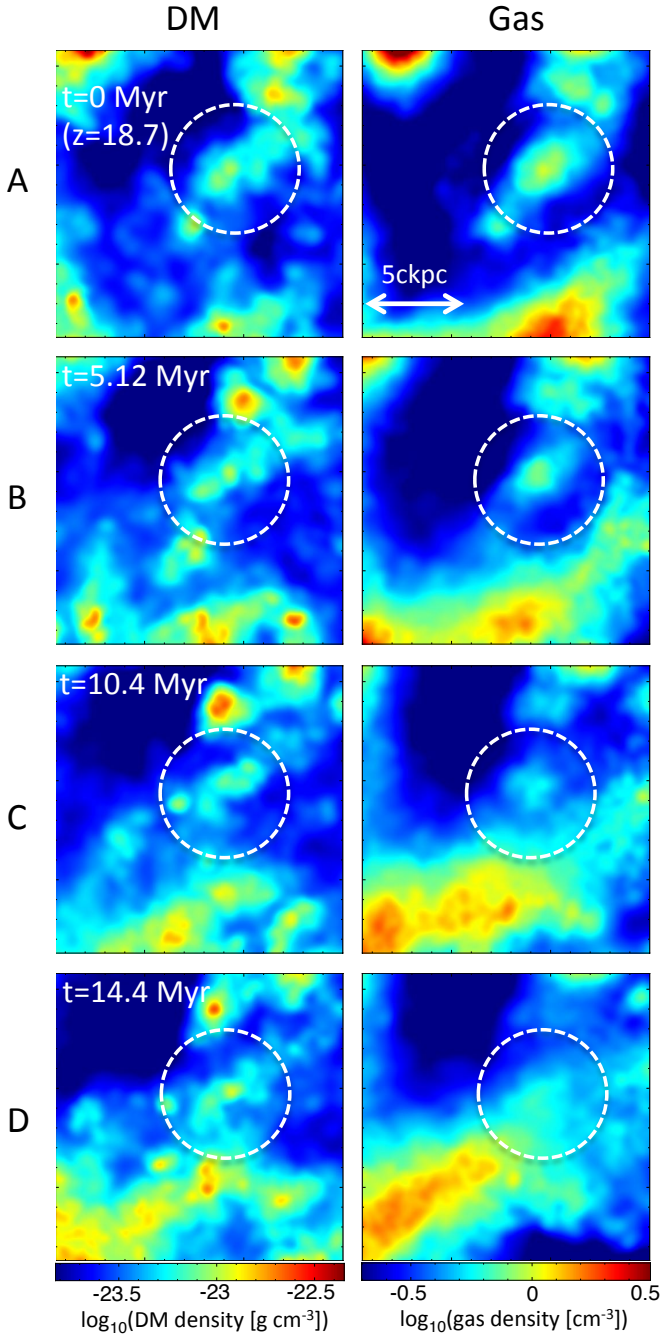


FIG. 7.— Time evolution of F2 halo at the four reference points shown in Figure 6(c). Left: the projected DM density distributions. The large clump at the top left corner in each panel is the source halo. The candidate halo is inside the white dashed circle. The color scale represents the DM density. Right: the projected gas density around the candidate halo, the same region as in the left column. The color scale represents the gas density. The elapsed time t since the epoch of panels A is attached to each panel.

Pop III star formation even when $T_{\text{vir}} > 2000$ K. The halo temperature increases from $T_{\text{vir}} = 2000$ to 8000 K in $\simeq 50$ Myr, which is shorter by a factor of 2 than the same time duration for halo F1 (Section 4.1). The rapid growth of S1 is enabled by the major merger of two halos A and B, at $t \sim 0$. Figure 9(c) and (d) show that the density increases monotonically and that the tidal radius becomes equal to the virial radius of the halo right af-

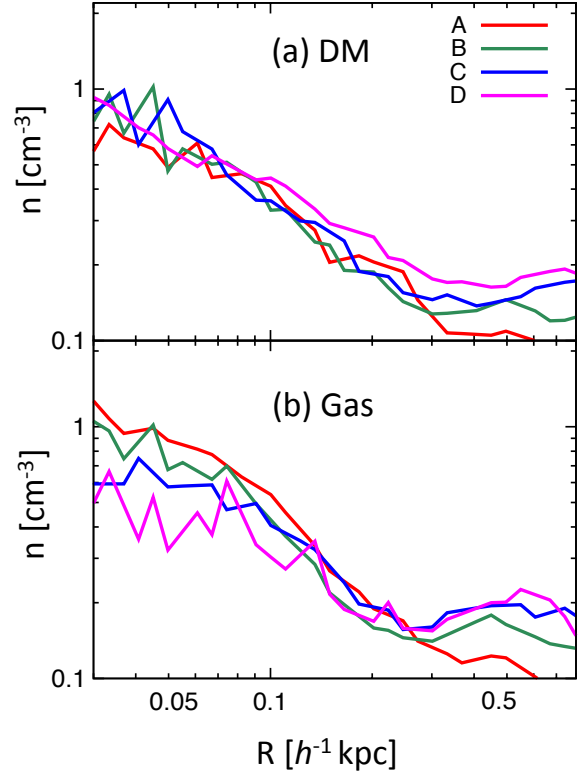


FIG. 8.— Density profiles of the (a) DM and (b) baryons for the F2 halo at the four reference points shown in Figure 6(c). The horizontal axis shows the distance from the density maxima of the cloud. Here the DM density is converted to the corresponding baryon density by $n_{\text{DM}} \equiv f_b \rho_{\text{DM}} / (1.2 m_p)$, where 1.2 is the mean molecular weight of the neutral gas.

ter the major merger. The cloud is able to collapse even under the strong tidal field.

Gravitational collapse can be induced not only by the self-gravity of the gas cloud but also by the gravity of the DM halo. The DM density profile of the candidate halo, $\rho_{\text{DM}}(r)$, follows a simple relation with the gas density $\rho(r)$ as $\rho_{\text{DM}}(r) = \Omega_m / \Omega_b \rho(r)$ when the density is less than 100 cm^{-3} (Choi et al. 2015). The radius R_{grav} of an isothermal cloud that experiences gravitational collapse is estimated by the ratio of the enclosed mass to the local Bonnor–Ebert mass, defined as follows:

$$M_{\text{BE}} \equiv \frac{1.18 f_b^{1/2} c_s^4}{p^{1/2} G^{3/2}} \geq \int_0^{R_{\text{grav}}} [\rho_{\text{DM}}(r) + \rho(r)] 4\pi r^2 dr, \quad (18)$$

where c_s is the local sound speed, $f_b \equiv \Omega_b / \Omega_m$, and p is the pressure of the cloud. The factor f_b explains the effect of the DM potential. In the derivation of eq. (18), the gravitational force originating from the matter outside the virial radius of the halo is neglected. We use the Bonnor–Ebert mass because the cloud is approximately static before the onset of the collapse.

Figure 10(a) compares the evolution of gravitational radius R_{grav} and tidal radius R_{tid} . Just before $t \sim 0$, $R_{\text{grav}}/R_{\text{vir}}$ drops almost by an order of magnitude. When R_{grav} is much smaller than R_{tid} , the cloud can collapse without being disrupted by the light source halo. In the case of F1, R_{grav} becomes larger than R_{tid} at $t \sim 0$, so that the cloud cannot collapse because of the strong tidal

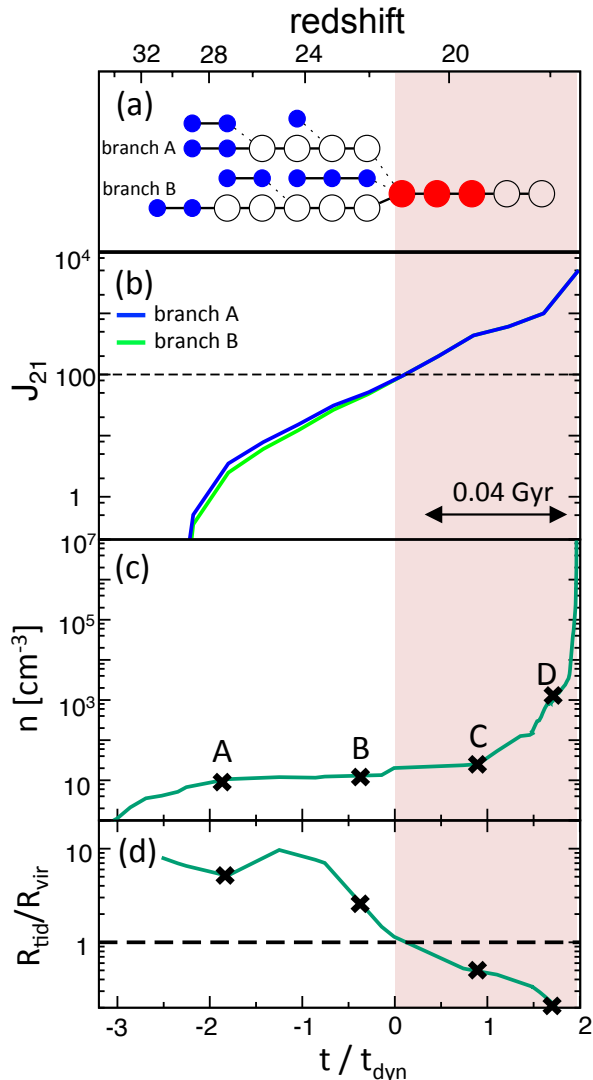


FIG. 9.— Same as Figure 4 but for case S1. There are two main branches (A and B) in the merger tree, and the DC candidate halo is the product of the major merger of these two branches. The solid blue and green lines in panel (b) show the evolution of the LW intensity at the halo center of branches A and B. The reference dynamical time at $t = 0$ is $t_{\text{dyn}} = 26.9$ Myr.

force (Fig. 10b).

The right panels of Figure 11 exhibit how successive mergers take place to lead to DC. Six clumps are finally merged into a clump at C. Before the merger, the mean temperature of the clouds is $\simeq 4000$ K (left column of Fig. 11). It finally settles at $\simeq 8000$ K at C. The rapid temperature increase is caused by the strong shock generated by the merger and enables efficient atomic hydrogen cooling. Radiative cooling then reduces the pressure support, promoting the collapse of the cloud. Interestingly, the two clumps merge at a relative velocity of 23.0 km s^{-1} , which is nearly twice the sound speed of the cloud.

The major merger also concentrates matters toward the halo center. Figure 12 shows the total enclosed mass within the distance R from the halo center before (dashed) and after the merger (black solid). The mass increases by an order of magnitude at $R \sim 0.1$ kpc. After

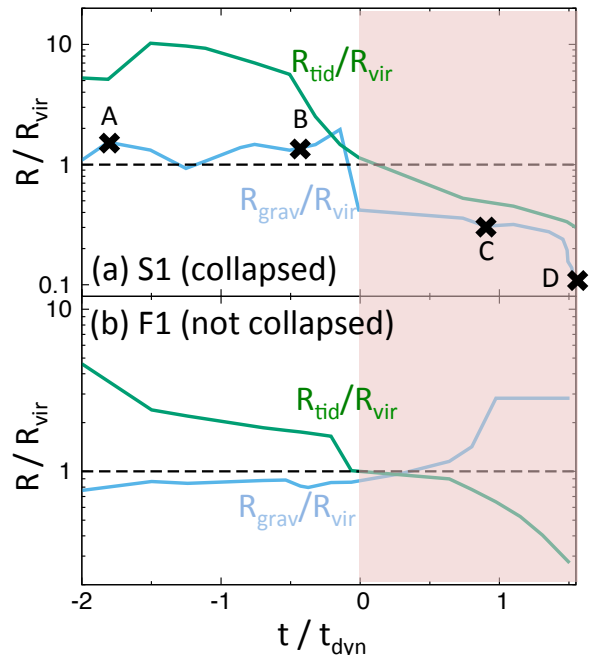


FIG. 10.— Evolution of gravitational radius (eq. 18) relative to the virial radius (blue) and the tidal radius relative to the virial radius (green) for (a) S1 and (b) F1. The time origin $t = 0$ is set to be the moment at which the halo satisfies the DC criteria, and the time is normalized by the dynamical time at $t = 0$.

the merger, the enclosed mass exceeds M_{BE} (red curve in Fig. 12) at $R \sim 0.1$ kpc. This induces the gravitational instability. Thus, the major merger also causes a sudden decrease of R_{grav} by an order of magnitude (Fig. 10).

Major mergers increase the central density of the cloud, while the minor mergers act in the opposite way as shown in Section 4.1. Within the cloud core, the gravitational force dominates over the pressure force and over the tidal forces exerted by neighboring halos. Apparently the mass of the extended core determines whether the cloud expands or contracts. We will discuss this issue more in detail in Section 6.2, where we quantify the core entropy as a proxy to the collapse criteria.

4.3.2. The evolution of S2

The cloud in S2 also collapses in essentially the same manner as S1. There are two notable differences, however. One is that the major merger occurs about one dynamical time after when the halo satisfies the DC criteria. Hence the merger acts as promoting the collapse. The other is that the closest light source halo has a similar mass to S2. It exceeds the atomic-cooling threshold 20 – 30 Myr earlier than S2 itself. Apparently our S2 is a similar system to the “synchronized pair” studied in Visbal et al. (2014b), where the source halo and the main DC halo become atomic-cooling halos simultaneously. In the case of S2, there is another luminous halo, which contributes more than half of the total J_{21} at S2.

The mass of the closest light source halo is not large enough to cause significant tidal effects on the main DC halo. We find that R_{vir} remains smaller than R_{tid} over one dynamical time after the halo satisfies the DC criteria. The central density remains high and the cloud ‘survives’ against disruption until the final merger trig-

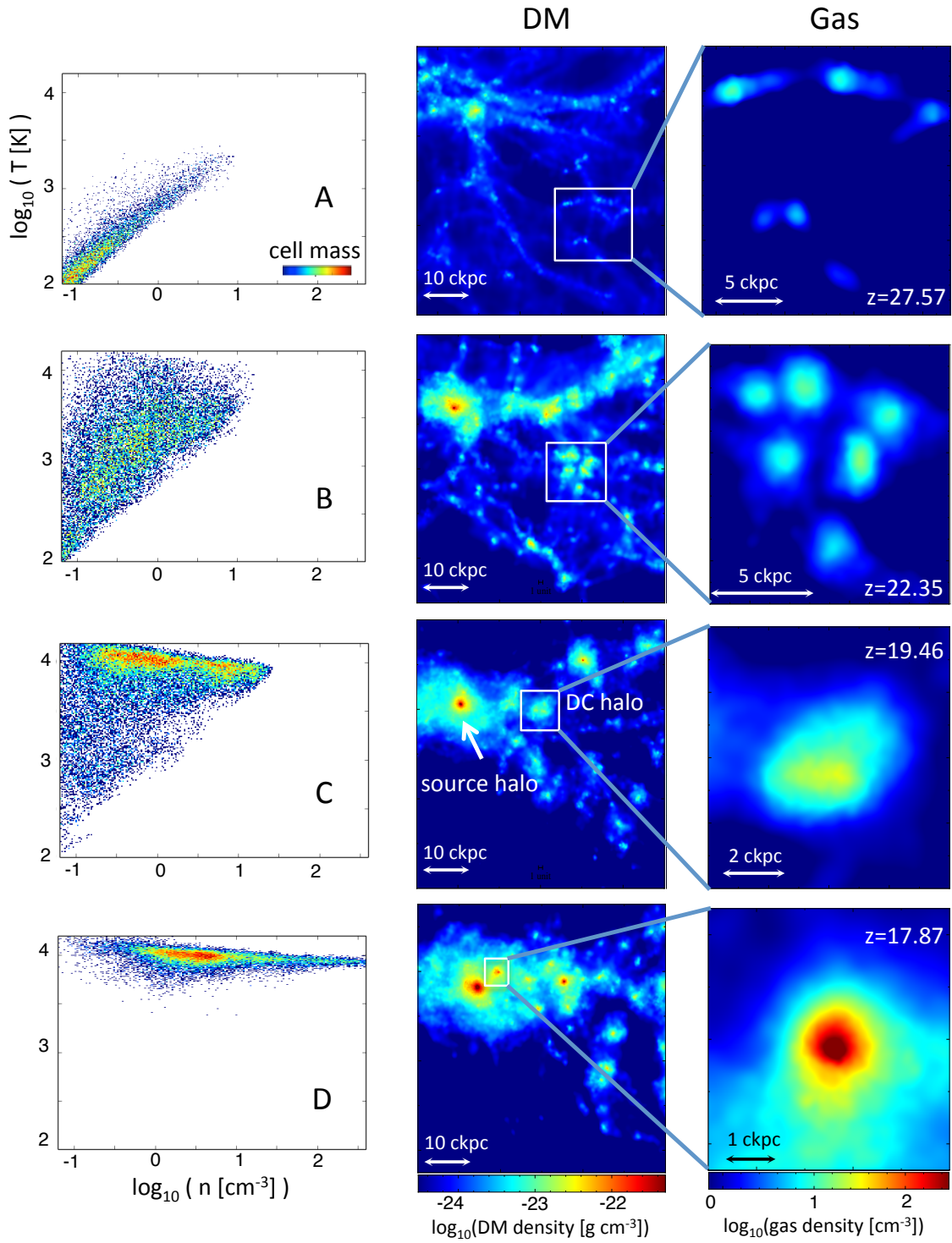


FIG. 11.— Same as Figure 5, but for four reference points for case S1 shown in Figure 9. There are six small clumps in epochs A and B that are merged into the DC candidate halo in epochs C and D.

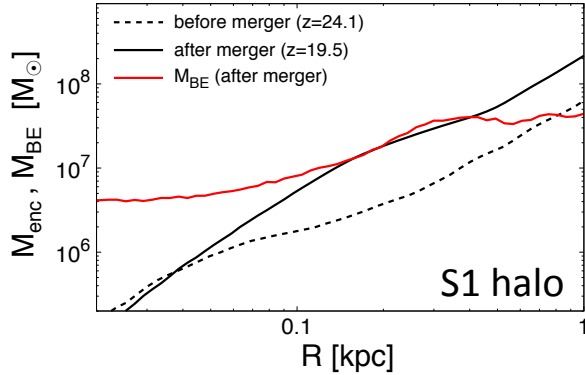


FIG. 12.— Radial profiles of the enclosed mass before ($z = 24.1$; black dashed) and after the major merger ($z = 19.5$; black solid). The red solid line shows the profile of the Bonnor–Ebert mass after the merger.

gers DC.

4.4. Thermal Evolution of DC Gas Clouds

We aim at deriving general features in the evolution of DC clouds. Figure 13(a) shows the density evolution of the DC candidate halos. We plot the evolution until each host halo merges with its nearby light source halo. For the low- z samples (green lines) that satisfy the DC criteria at $z < 17$, the density peaks at $n = 1 - 3 \text{ cm}^{-3}$ at $t \sim 0$, but gradually decreases afterward. The high- z samples (blue lines) at $z > 17$ have relatively higher densities than the low- z samples owing to the cosmic expansion. By performing high-resolution hydrodynamic simulations, we are able to robustly determine whether or not DC is triggered in the candidate halos.

Figure 13(b) shows the temperature evolution as a function of density. At the beginning of the collapse, the density and temperature evolve adiabatically as $T \propto n^{2/3}$. The temperature rises monotonically to $T \simeq 8000 \text{ K}$, tracing roughly the halo virial temperature. At $T > 1000 \text{ K}$, the evolution deviates upward from the adiabatic track because of dynamical heating associated with mergers. The entropy monotonically increases because radiative cooling is inefficient until the temperature reaches 8000 K .

The density of the uncollapsed cloud reaches only $\sim 10 \text{ cm}^{-3}$. The Jeans length at the maximum density and at $T = 8000 \text{ K}$ is $10^2 - 10^3 \text{ pc}$, which is comparable to the virial radius of the host halo. In the case of F1, the tidal force at the virial radius becomes very strong because the DC halo approaches the light source halo rapidly before the onset of the collapse. We will show that similar evolution is seen in many of the other uncollapsed cases in Section 6.1 below.

5. FORMATION OF A PROTOSTAR

For S1 and S2, we continue the calculations until the central density reaches 10^8 cm^{-3} . In both the cases, the target gas cloud approaches quickly, while contracting, to the light source halo. The bottom left panel of Figure 14 shows a schematic picture of the orbit of the S1 halo relative to the light source halo. The cloud is attracted gravitationally and passes by the light source. Figure 14 also shows the projected gas density around the DC halo at $t = 48.9, 52.3,$ and 52.7 Myr . The bottom right panel

($t = 48.9 \text{ Myr}$) corresponds to the reference point D in Figure 9.

The DC conditions are satisfied at $t = 0$. At $t = 48.9 \text{ Myr}$, the cloud is almost spherical while it is tidally distorted at $t = 52.3 \text{ Myr}$. The cloud approaches 100 pc from the light source halo at $t = 52.3 \text{ Myr}$. During the passage of the pericenter, the density increases and reaches 10^8 cm^{-3} quickly. Figure 15 shows gas density profiles at the three output times. The density evolves self-similarly (Larson 1969; Penston 1969), but is perturbed tidally at $R \simeq 4 \text{ pc}$.

It is worth noting that, once the density exceeds $\simeq 3 \times 10^3 \text{ cm}^{-3}$ with $T = 8000 \text{ K}$, H_2 cooling never becomes efficient (Inayoshi & Omukai 2012). The regime is called “zone of no return”, where collisional dissociation rapidly destroys H_2 molecules. In our calculation, the cloud enters the zone at $t \simeq 48.9 \text{ Myr}$, after which H_2 cooling cannot operate in a contracting gas.

It is important to estimate the mass of an SMS to be formed in the gas cloud S1 and S2. As a rough estimate, we calculate the Jeans mass and find that it is comparable to the enclosed gas mass at $M(< R) \sim 10^5 M_\odot$, with a negligible contribution of DM. Hence, the gas is self-bound and is going to collapse. Figure 16 shows the radial distribution of the mass infall rate $\dot{M} \equiv 4\pi R^2 \rho(R) v_{\text{in}}(R)$ for S1 (red) and S2 (blue) when the central density reaches $2 \times 10^7 \text{ cm}^{-3}$. Here, $v_{\text{in}}(R)$ is the radial infall velocity component. We suppose that a protostar will accrete the surrounding gas approximately at the instantaneous mass infall rate. The expected mass infall rates are $0.1 \sim 1 M_\odot \text{ yr}^{-1}$ at $10^3 M_\odot \lesssim M \lesssim 10^5 M_\odot$ for S1 and S2. At $M \gtrsim 10^5 M_\odot$, however, the mass is outflowing from the cloud because the tidal force strips the gas in the halo outskirts.

The obtained \dot{M} is very large, as expected in the DC model. We infer the final stellar mass of the SMS without following the evolution in the accretion stage. The stellar evolution calculations show that the stellar envelope inflates with such rapid mass accretion (e.g., Omukai & Palla 2003; Hosokawa et al. 2012). The stellar effective temperature is fixed nearly at $\simeq 5000 \text{ K}$ in the so-called supergiant stage. As a result, the emissivity of ionizing photons is greatly reduced (e.g., Hosokawa et al. 2013; Schleicher et al. 2013; Sakurai et al. 2015). The radiative feedback will be too weak to halt the mass accretion, so that the star finally accretes almost all the infalling gas. The estimated mass from the infalling rate is $2 \times 10^5 M_\odot$ for S1 and $3 \times 10^5 M_\odot$ for S2.

We follow the collapse of the DC clouds until the central density reaches 10^8 cm^{-3} . The angular momentum could arise as a barrier against the collapse, potentially decelerating the collapse to cause gravitational fragmentation. However, numerical simulations show that the clouds do not have such high angular momentum because of the gravitational torque caused by the nonaxisymmetric structure of the host DM halo (Choi et al. 2015; Shlosman et al. 2016; Luo et al. 2016). Once the collapse begins, vigorous fragmentation does not occur until an embryo protostar forms (Inayoshi et al. 2014; Latif et al. 2016, e.g.). We have run two additional simulations to higher densities. Our preliminary simulations also show that our DC clouds, S1 and S2, also continue to collapse until reaching $n \sim 10^{13} \text{ cm}^{-3}$ without frag-

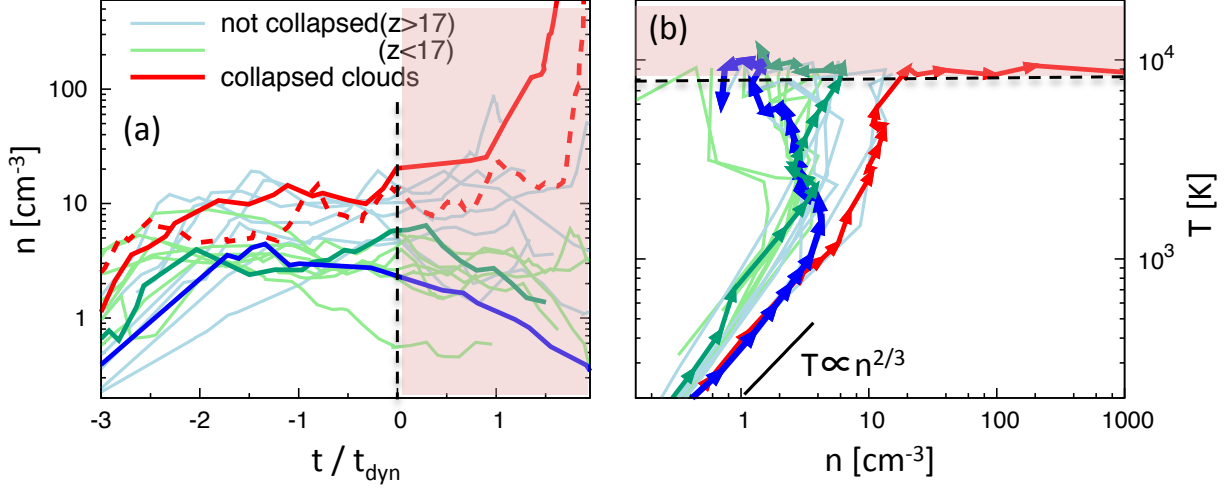


FIG. 13.— Time evolution of 16 gas clouds hosted by DC candidate halos. (a) Evolution of the central density n as functions of time t . We mark the four representative cases with thick lines: F1 (green), F2 (blue), S1 (red solid), and S2 (red dashed). The blue and green lines represent the uncollapsed clouds that satisfy the DC criteria at $z > 17$ and at $z < 17$, respectively. At the end of each line, the target halo is merged with the light source halo, except for the collapsed clouds. (b) Temperature evolution as a function of the density for the 15 representative cases (S2 is not shown because it follows almost the same path as for S1). For the other 12 DC clouds, we only show the evolution paths on the plane, and the evolution is smoothed out for every t_{dyn} . The black solid line shows the adiabat, $T \propto n^{2/3}$. In each panel, the shaded region indicates $T_{\text{vir}} > 8000$ K, where atomic hydrogen cooling becomes efficient.

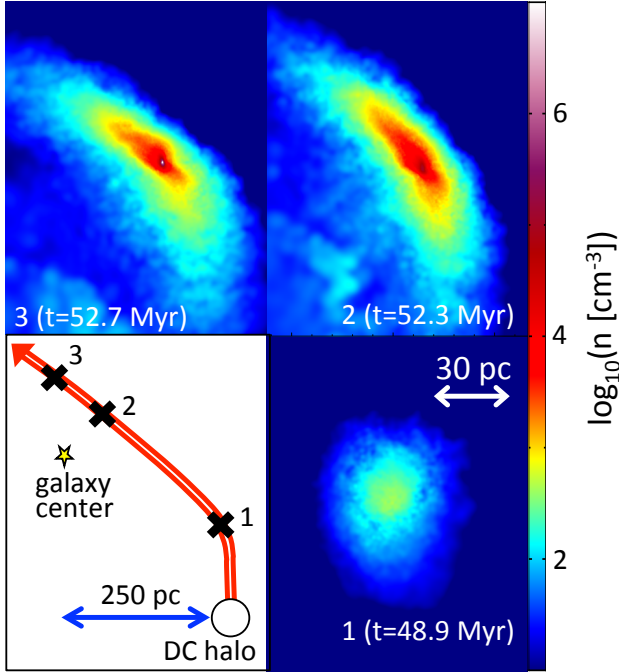


FIG. 14.— Bottom left: the schematic picture of the locus of the S1 halo relative to the source halo. The red arrow shows the path of the DC halo relative to the light source halo. Bottom right, top right, top left: The projected gas density map around the DC halo. The panels show the cloud’s snapshots at $t = 48.9$, 52.3 , and 52.7 Myr counterclockwise, corresponding to the points 1, 2, and 3 in the bottom left panel. The time origin represents the epoch when the halo meets the DC criteria.

mentation. The fragmentation will occur more often in the late stage of the protostellar accretion owing to the gravitational instability of a circumstellar disk (e.g., [Becerra et al. 2015](#); [Sakurai et al. 2016](#)). To know whether the formation of a $10^5 M_{\odot}$ star is possible, we have to

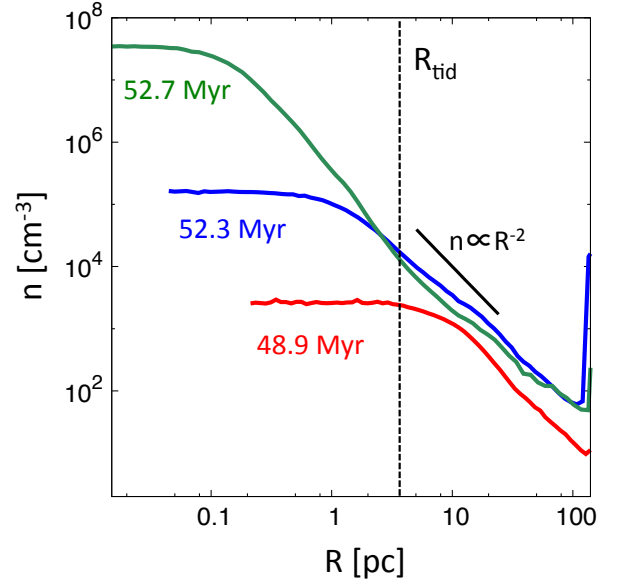


FIG. 15.— Radial profiles of the gas density in the S1 halo at $t = 48.9$, 52.3 , and 52.7 Myr. The dashed line indicates the tidal radius at which the tidal force exceeds the self-gravity of the gas cloud at $t = 52.7$ Myr.

follow a long-term evolution with accretion. This is beyond the scope of this paper and will be studied in our next work.

6. CLOUD COLLAPSE UNDER STRONG TIDAL FIELD

In this section, we quantitatively study the tidal effect on the evolution of DC candidate halos. Throughout this section, we refer to a candidate halo as the “target”, while a halo that is emitting H₂ dissociation radiation is referred to as the “source”.

We first consider how strong the tidal force is at the virial radius R_{vir} of the target halo, which we compare

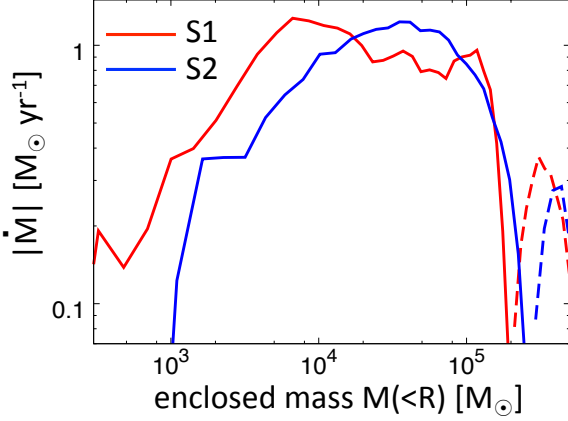


FIG. 16.— Expected mass infall rates $|\dot{M}| = 4\pi r^2 \rho |v|$ as functions of the enclosed mass $[M(< R)]$. The snapshots when the central density reaches $2 \times 10^7 \text{ cm}^{-3}$ are used to define the profiles. We plot the profiles for S1 (red) and S2 (blue). The solid lines show the infall rates, while the dashed lines show the outflow rates.

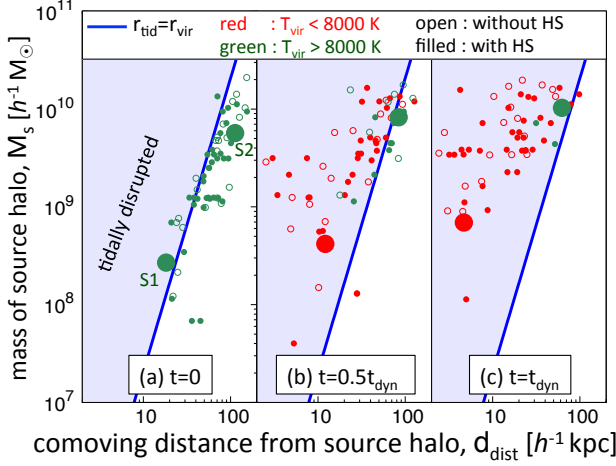


FIG. 17.— Time evolution of the source halo mass M_s and the comoving distance between the candidate and source halos d_{dist} for all 68 candidate halos. Panels (a), (b), and (c) show the snapshots at the different epochs $t = 0$, 0.5 , and $1.0 t_{\text{dyn}}$, respectively. The candidate halo satisfies the DC criteria at $t = 0$. The symbol colors represent the halos with $T_{\text{vir}} < 8000 \text{ K}$ (red) and $> 8000 \text{ K}$ (green). The filled and open circles show whether the hydrodynamical simulations (HS) are performed or not. The halos that host the collapsed clouds (S1 and S2) are shown with the larger circles. In each panel, the shaded area denotes $R_{\text{tid}} < R_{\text{vir}}$, i.e., the tidal force is strong enough to disrupt the halo envelope. The solid line represents the critical points for $R_{\text{tid}} = R_{\text{vir}}$.

with the tidal radius given in eq. (15). The tidal force by the source halo gets stronger as the target halo approaches. Thus, the cloud (in the target halo) collapses within an infalling timescale after the target halo satisfies DC criteria.

6.1. Evolution of Tidal Radius

We plot the time evolution of the source halo mass and separation between the source and target halos in Figure 17. Each panel shows the snapshot at (a) $t = 0$, (b) 0.5 , and (c) $1.0 t_{\text{dyn}}$ after the target halo satisfies the DC criteria. The shaded region indicates $R_{\text{tid}} < R_{\text{vir}}$, where the outer part of the candidate halo is subject to the tidal force from the source halo.

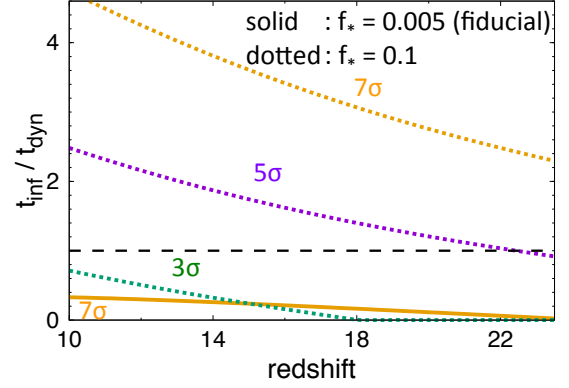


FIG. 18.— Infall time of the target halo from d_{LW} (eq. 20) to d_{tid} (eq. 21) normalized by the dynamical time at each redshift. The lines represent the evolution for the source halos that are formed from 3σ (green), 5σ (purple), and 7σ (orange) initial density peaks. The solid and dotted lines are for the fiducial and enhanced star formation efficiency, $f_* = 0.005$ and 0.1 , respectively. The other two cases with 3σ and 5σ are not shown because d_{LW} is always smaller than d_{tid} . The horizontal dashed line indicates $t_{\text{inf}} = t_{\text{dyn}}$.

In most of the cases, the virial temperature of the halo falls below 8000 K as they approach the source halo. The target halo loses its mass by tidal disruption, and the gas cloud does not collapse. Clearly, the tidal disruption prevents the clouds from collapsing. The target halos fall in faster than collapsing. With our model of a UV-emitting galaxy, the LW intensity at the position of the target halo at distance d_{dist} from the source halo is given by (Iliev et al. 2005);

$$J_{21} = 63 \left(\frac{M_{\text{source}}}{10^9 M_{\odot}} \right) \left(\frac{f_{\gamma}}{2.0} \right) \left(\frac{f_{J21}}{0.4} \right)^{-1} \left(\frac{20 \text{ Myr}}{t_s} \right) \left(\frac{1 \text{ kpc}}{d_{\text{dist}}} \right)^2, \quad (19)$$

where t_s is the mean lifetime of UV-emitting stars in the source halo, f_{J21} is the fraction of the LW intensity originating from the closest luminous halo to the total LW intensity, f_{γ} is defined as $f_{\gamma} \equiv f_* f_{\text{esc}} N_i$, where f_* is the star formation efficiency, which is the baryon fraction converted to stars, f_{esc} is the escape fraction of the UV photons, and N_i is the number of the emitted photons per unit stellar mass throughout the mean lifetime t_s . We take the fiducial value of $f_{\gamma} = 2$ (Iliev et al. 2007) and $f_{J21} = 0.4$. The latter choice is motivated by the result of our semianalytical model (Section 2.3).

Equation (19) gives the critical distance d_{LW} , within which the target halo is irradiated by sufficiently strong LW radiation for DC. With standard normalizations, the critical distance is given by

$$d_{\text{LW}} = 0.2 \text{ kpc} \left(\frac{M_{\text{source}}}{10^8 M_{\odot}} \right)^{1/2} \left(\frac{f_{\gamma}}{2} \right)^{1/2} \left(\frac{f_{J21}}{0.4} \right)^{-1/2} \left(\frac{20 \text{ Myr}}{t_s} \right)^{1/2} \left(\frac{100}{J_{21}^{\text{crit}}} \right)^{1/2}. \quad (20)$$

The distance at which the tidal radius is equal to the

virial radius, d_{tid} , can be estimated by eq. (15) as

$$d_{\text{tid}} = 0.524 h^{-1} \text{ kpc} \left(\frac{M_{\text{source}}}{10^8 h^{-1} M_{\odot}} \right)^{1/3} \left(\frac{10}{1+z} \right), \quad (21)$$

where z is the redshift under consideration.

A cloud can collapse when it lies in $d_{\text{tid}} < d_{\text{dist}} < d_{\text{LW}}$, if the collapse is initiated at the virial radius. Because the source halo also grows in mass, the ratio of d_{LW} to d_{tid} becomes larger and the target halo might spend for a longer time in $d_{\text{tid}} < d_{\text{dist}} < d_{\text{LW}}$, because $d_{\text{LW}} \propto M_{\text{source}}^{1/2}$ while $d_{\text{tid}} \propto M_{\text{source}}^{1/3}$.

We evaluate the infalling time for the target halo moving from d_{LW} to d_{tid} , considering the infalling velocity at d_{LW} . Detailed derivations based on a spherical collapse model are given in Appendix B. The derived infall time t_{inf} is determined by the source halo mass but independent of the mass of the target halo.

Figure 18 shows the infalling time t_{inf} for the source halo formed in 3σ (green), 5σ (purple), and 7σ (yellow) peaks of the initial density field. The solid line corresponds to the case with the fiducial parameters used in our semianalytical model. We select 3σ – 4σ regions, so the candidate halos should be disrupted by the tidal force from the source halo before they collapse, aside from a few exceptions for which the major merger accelerates the collapse. Even for a 7σ halo, which is as rare as the observed high- z QSOs ($\sim \text{Gpc}^{-3}$), t_{inf} is much smaller than t_{dyn} . The dashed lines show the infalling time of the target halo under the enhanced star formation efficiency $f_* = 0.1$, much larger than the typical value $f_* = 0.005$. This is the highest value of f_* allowed to explain the observed galaxy luminosity functions at $z \sim 6$ – 7 (Agarwal et al. 2012). The infalling time t_{inf} can exceed t_{dyn} in higher-density peaks, while they remain to be of an order of unity even for 7σ peaks in the shown redshift range. This fact implies that the tidal force still has some impact on the collapse of the target halo because t_{inf} remains comparable to t_{dyn} .

The above discussions are only concerned with the tidal force at the virial radius. When an infalling cloud begins collapsing near the virial radius of the target halo, it approaches the source halo so fast that the tidal force becomes strong and prevents the collapse. Therefore, for a cloud to experience DC, gravitational instability needs to take place well within the inner part of the target halo, where the tidal effect from the source halo is weak.

6.2. Onset of the Cloud Collapse

The DC (candidate) clouds evolve adiabatically, without significant radiative cooling, until the gas temperature reaches 8000 K because H_2 cooling is inefficient. It is known that a gas cloud contracting adiabatically develops a universal entropy profile, as studied in the context of the formation of galaxy clusters (e.g., Voit et al. 2003, 2005). In spite of the enormously different mass scale, our simulated gas clouds hosted by the DC candidate halos also show such universal features (see also Visbal et al. 2014a).

The entropy of an ideal gas is defined by the thermodynamical quantities as

$$K = k_{\text{B}} T n_{\text{b}}^{-2/3}, \quad (22)$$

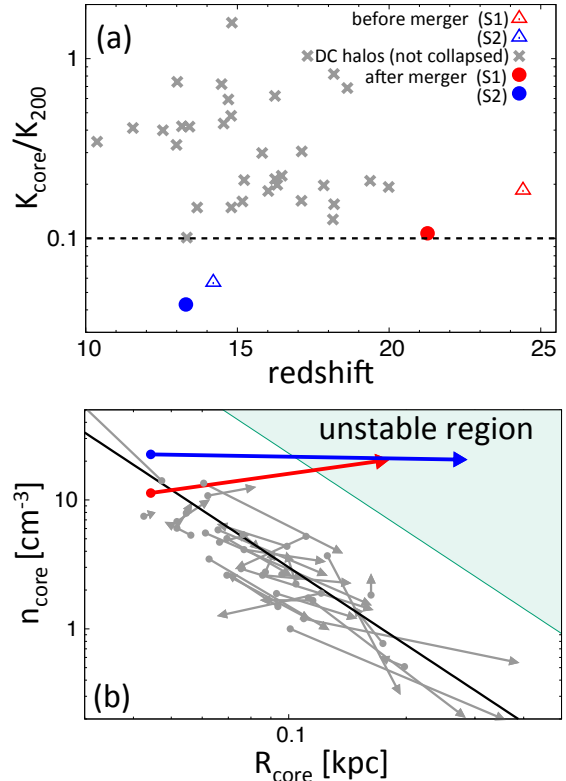


FIG. 19.— (a) Entropy of the cloud core normalized by K_{200} (eq. 23). The colored symbols denote the collapsed halos S1 (red) and S2 (blue), whereas the gray symbols show the uncollapsed clouds. The open and filled symbols represent the entropy of collapsed clouds before and after the major merger, respectively. The dashed line shows the mean value of the entropy by the universal profile. (b) Evolution of the core radius and number density after the host halo satisfies the DC criteria. The start (filled circle) and end points of each arrow represent the core properties when the halo meets the DC criteria and t_{dyn} after that moment, respectively. The black solid line shows the analytical core radius-density relation given by eq. (26). The cloud becomes gravitationally unstable in the shaded region, satisfying eq. (27).

where k_{B} is the Boltzmann constant, T is the temperature, and n_{b} is the baryon number density. We can also define a “halo entropy” as

$$K_{200} = k_{\text{B}} T_{\text{vir}} (200 \bar{n}_{\text{b}})^{-2/3}, \quad (23)$$

where \bar{n}_{b} is $\Omega_{\text{b}}/\Omega_{\text{m}}$ times the mean matter density of the universe. The entropy profile of the cloud consists of two parts, a constant entropy core and an outer envelope with $K \propto (r/r_0)^{1.1}$. Under the adiabatic collapse, the core radius and entropy are approximately given as $R_{\text{core}} \sim 0.1 R_{\text{vir}}$ and $K_{\text{core}} \sim 0.1 K_{200}$, respectively (Visbal et al. 2014a). We find that our DC clouds roughly follow this universal profile. Figure 19(a) shows K_{core} of the candidate halos just after they satisfy the DC criteria. The halos have slightly larger entropies than $0.1 K_{200}$ but show little redshift dependence. It is interesting that the two successful cases, S1 (red) and S2 (blue), have the smallest entropies after the major merger. Figure 19(b) plots the evolution of all the DC clouds in the $n_{\text{core}} - R_{\text{core}}$ from the time when the halo meets the DC criteria (initial point) to t_{dyn} after that moment. The evolution is depicted by the arrows in the figure. We define R_{core} as the radius at which the density is half of the maximum density at the center. If we approximately set

$K_{\text{core}} = 0.1K_{200}$ and $R_{\text{core}} = 0.1R_{\text{vir}}$, the core properties can be given as follows (Inayoshi et al. 2015):

$$R_{\text{core}} = 0.1R_{\text{vir}},$$

$$= 35 h^{-1} \text{ pc} \left(\frac{T_{\text{vir}}}{10^4 \text{ K}} \right)^{3/2} \left(\frac{1+z}{16} \right)^{-3/2}, \quad (24)$$

$$n_{\text{core}} = \left(\frac{K_{\text{core}}}{K_{200}} \right)^{-3/2} \bar{n}_{\text{b}} = 22 \text{ cm}^{-3} \left(\frac{1+z}{16} \right)^3. \quad (25)$$

By assuming $T_{\text{vir}} = 8000 \text{ K}$, we can get an analytical estimate

$$n_{\text{core}} = 0.03 \text{ cm}^{-3} \left(\frac{R_{\text{core}}}{1 \text{ kpc}} \right)^{-2}. \quad (26)$$

The estimates are in good agreement with the core properties of our sample (Figure 19b).

For a gas cloud to collapse, the core mass should be larger than the Bonnor–Ebert mass (eq. 18). The core mass can be estimated by $\sim R_{\text{core}}^3 \rho_{\text{core}}$, and thus the gravitational instability condition can be written as

$$n_{\text{core}} > 0.23 \text{ cm}^{-3} \left(\frac{R_{\text{core}}}{1 \text{ kpc}} \right)^{-2}, \quad (27)$$

which is shown by the shaded region in Figure 19 (b). Note that this critical density is an order of magnitude higher than the actual core densities. Figure 19(b) shows that most of the candidate halos, except for the two successful cases, lie in the stable region, even one dynamical time after the gas starts cooling. Clearly, the core density needs to remain large to trigger DC.

We have seen that, in the cases of S1 and S2, the gas cloud collapse is driven by major mergers. The high-speed mergers with relative velocity of $v_{\text{rel}} \sim 2c_s$ generate shocks and increase the gas entropy. As shown in Figure 19(b), the mergers increase not only the core density but also the core size by an order of magnitude. The S1 and S2 gas clouds move into the gravitationally unstable region depicted in the figure.

Here we summarize the discussion in this section. An adiabatically contracting gas cloud has a universal entropy profile composed of a core and an envelope. For the DC gas clouds in our simulation, the core does not contain a large enough mass to gravitationally collapse. The core would gain further mass through accreting the surrounding gas, but the host halo itself is tidally disrupted quickly within one dynamical time. Gravitational collapse is often completely halted. The only “successful” path found in this paper is the sudden increase of the core mass by major merger events. We have found that the successful DC systems in our samples indeed experience major mergers.

7. DISCUSSION

7.1. Critical LW Intensity for DC

We have adopted a constant value of $J_{21}^{\text{crit}} = 100$ as our fiducial critical value for Pop II sources (Shang et al. 2010). We have also shown that the LW intensity at a cloud’s position varies with time as it approaches the

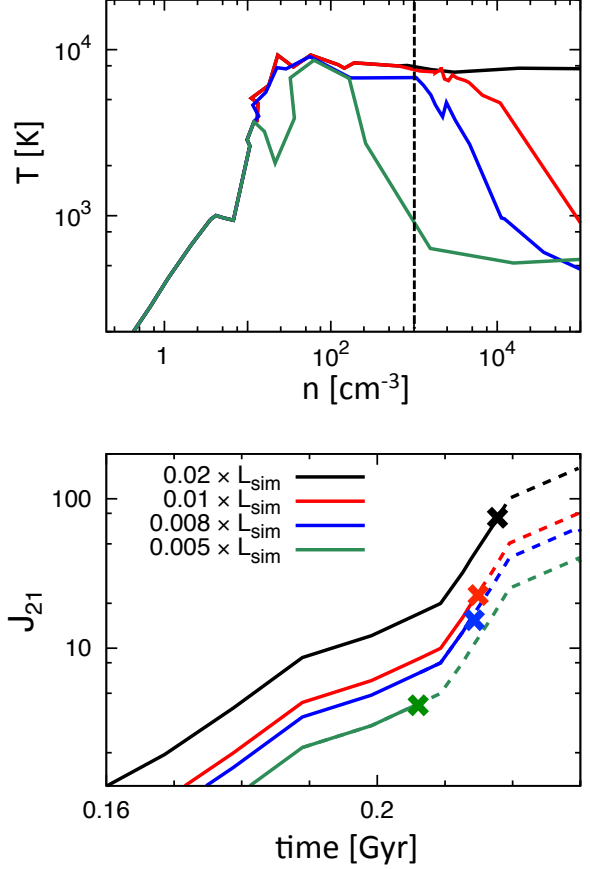


FIG. 20.— (a) Thermal evolution of the collapsing cloud S1 with the smaller LW luminosities of the light source halo: 0.5% (green), 0.8% (blue), 1% (red), and 2% (black) of the original value. (b) Time evolution of J_{21} for the same cases. The crosses indicate the epochs when the cloud density has reached $n_{\text{LTE}} = 10^3 \text{ cm}^{-3}$. The dashed line shows the evolution of LW intensity for $n > n_{\text{LTE}}$.

light source halo. It is important to reexamine in detail the critical intensity J_{21}^{crit} for DC.

Whether or not a gas cloud evolves along the atomic-cooling track is determined by the LW intensity when the gas density reaches $n_{\text{LTE}} \sim 10^3 \text{ cm}^{-3}$, the critical density for the H_2 rovibrational transitions (e.g., Omukai 2001; Shang et al. 2010). In order to study the effect of a time-dependent LW radiation field, we perform several test simulations based on our sample S1.

We record the time evolution of the LW luminosity of the light source halo $L_{\text{sim}}(t)$ in the original case S1. We then follow the collapse of the same gas cloud, reducing the source LW luminosity to 0.5%, 0.8%, 1%, and 2% of the original $L_{\text{sim}}(t)$. Note that, for all these cases, the LW intensities at the virialization are much lower than the normal critical value $J_{21}^{\text{crit}} \sim 100$. Figure 20(a) shows the evolution for the test cases. We see that even 2% of $L_{\text{sim}}(t)$ can lead to DC, whereas H_2 formation and cooling operate with 1% of $L_{\text{sim}}(t)$.

Figure 20(b) shows the time evolution of the LW intensity at the cloud core. The crosses indicate the epoch when the core density has reached $n_{\text{LTE}} = 10^3 \text{ cm}^{-3}$. The critical LW intensity at $n \sim n_{\text{LTE}}$ is between 20 – 80, which is comparable to J_{21}^{crit} obtained by Shang et al. (2010). We thus suggest that the critical LW intensity for DC should be evaluated at $n \sim n_{\text{LTE}}$, not at

the time of virialization. The figure also shows that a slight reduction of the source luminosity results in a dramatically lower value of $J_{21,n_{\text{LTE}}}$. With 0.5% of $L_{\text{sim}}(t)$, for instance, $J_{21,n_{\text{LTE}}}$ is lower by an order of magnitude than that with 2% of $L_{\text{sim}}(t)$, though the luminosity differs only by one-fourth. This is because, with 0.5% of $L_{\text{sim}}(t)$, the collapse advances earlier via efficient H_2 cooling when the cloud is located at a distant place from the source halo. Obviously, following both the cloud collapse in and around the virial radius and the halo assembly is necessary to derive the LW intensity at the critical density n_{LTE} .

Overall, the above results suggest that setting $J_{21}^{\text{crit}} \sim 100$ at the virialization is too strict for DC. In general, it takes a few dynamical times from the virialization until the density reaches $n \sim n_{\text{LTE}}$. During this period, J_{21} increases by an order of magnitude as the cloud approaches the light source halo. Therefore, moderate LW intensity at the epoch of the virialization, probably much lower than previously thought, is sufficient to induce DC.

This opens a possibility that a large number of DC halos may exist in the universe. For the DC halos in a realistic cosmological context, however, the exact value of J_{21}^{crit} at virialization actually depends on the subsequent evolution, which can be followed only by hydrodynamical simulations. Ultimately, we will need a number of hydrodynamics simulations with a large volume, with which we can find possibly more halos under the moderate LW fields $J_{21} \sim 10$. It is also necessary to follow the cloud collapse until the density reaches $n \sim 10^3 \text{ cm}^{-3}$ for each case.

7.2. Effects of Ionization Photons and X-Ray

We have only considered UV photons with energies below 13.6 eV because the mean free path of ionizing photons is much smaller than that of the LW photons. If a collapsed cloud approaches the vicinity of the light source halo, the cloud might be affected directly by ionizing photons.

The ionizing radiation enhances H_2 cooling, because the electrons catalyze the formation of H_2 via the H^- reaction path. The increase of the ionization degree accelerates the formation of H_2 and thus may prevent DC. In addition, X-ray photons produced by the light source have large mean free paths, which can have an impact on the evolution of the central core of the cloud (Inayoshi & Omukai 2011; Inayoshi & Tanaka 2015).

It is clearly important to address the impact of the ionizing photons and X-rays on the thermal evolution of DC clouds. To this end, we employ one-zone calculations and follow the evolution of the S1 cloud by including the effects of the additional radiation. We directly use the density evolution in our simulation because the cloud actually collapses over a much longer timescale than t_{ff} , while we assume that the collapse proceeds at a rate of t_{ff} when H_2 cooling is efficient. The density evolution can be described as

$$\frac{d\rho}{dt} = \begin{cases} \rho/t_{\text{ff}} & (\text{when } \text{H}_2 \text{ cooling is efficient}), \\ \dot{\rho}_{\text{sim}}(t) & (\text{otherwise}), \end{cases} \quad (28)$$

where $\dot{\rho}_{\text{sim}}(t)$ is the time derivative of the density of the cloud core in the simulation. Nonequilibrium chemistry and the energy equation are solved in the same manner

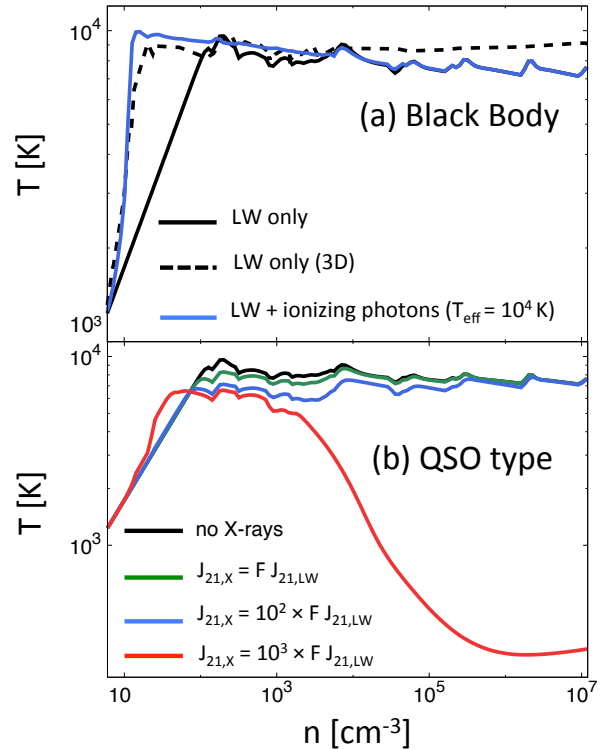


FIG. 21.— (a) Evolution of the temperature as the density rises with and without ionizing radiation. The black line represents the case without UV photons, and the blue line represents the evolution under the black body radiation with $T_{\text{eff}} = 10^4 \text{ K}$. The dashed line corresponds to the 3D simulation (S1), while the solid lines are the results of the one-zone calculation. In the presented one-zone models, we use the time evolution of the density taken from the 3D simulation (see eq. 28). The amplitude of radiation is the same as the normalization of the intensity at the LW bands, $J_{21,LW}$. (b) Evolution of the temperature as the density rises with and without X-rays of the QSO-type spectra, $J_{21} = J_{21,X}(\nu/\nu_0)^{-\alpha}$. The black line shows the evolution without the X-rays, while the green, blue, and red lines show the evolution with $J_{21,X} = 1, 10^2$, and $10^3 \times F J_{21,LW}$, respectively.

as in our 3D simulation described in Section 2.6. The column density N_i of each species i is given by

$$N_i = 0.5 \lambda_J n y_i, \quad (29)$$

where λ_J , n , and y_i are the Jeans length, the gas density, and the number fraction of the species i of the cloud core, respectively. The self-shielding against the ionizing photons and the secondary ionization are also considered, following Wolfire et al. (1995). The LW intensity is assumed to be the same as the intensity in the 3D simulation (S1).

We run the one-zone calculations for two different types of spectra: a black body spectrum with $T_{\text{eff}} = 10^4 \text{ K}$, and soft X-ray radiation with a power-law $J_{21} \propto J_{21,X}(\nu/\nu_0)^{-\alpha}$, with $h\nu_0 = 1 \text{ keV}$ and $\alpha = 1.8$. The conditions assumed above are, respectively, that the DC cloud is located within the Strömgren sphere around its light source halo and that the cloud is irradiated by X-ray radiation from the source. The spectrum resembles that of stars and QSOs, respectively. As for the QSO-type spectrum, we set the minimum and the maximum energy as $h\nu_{\text{min}} = 1 \text{ keV}$ and $h\nu_{\text{max}} = 10 \text{ keV}$.

The X-ray observations of local starburst galaxies show

a correlation between the X-ray luminosities and SFR (Glover & Brand 2003; Grimm et al. 2003):

$$L_X = 6.7 \times 10^{39} \left(\frac{\text{SFR}}{M_\odot \text{ yr}^{-1}} \right) \text{ erg s}^{-1}. \quad (30)$$

There is also a correlation between the LW luminosities and SFR (Inoue 2011):

$$L_{\text{LW}} = 1.14 \times 10^{43} \left(\frac{\text{SFR}}{M_\odot \text{ yr}^{-1}} \right) \text{ erg s}^{-1}. \quad (31)$$

By eliminating SFR in the above two observational correlations, we obtain the relation between the intensity in the LW bands $J_{21,\text{LW}}$ and $J_{21,\text{X}}$ as follows (Inayoshi & Tanaka 2015):

$$J_{21,\text{X}} = 5.7 \times 10^{-6} J_{21,\text{LW}} \equiv F J_{21,\text{LW}}. \quad (32)$$

Figure 21(a) shows the evolution with the stellar radiation case. We normalize the ionization radiation intensity at the Lyman limit, J_{UV} , to be J_{21} . Due to ionization heating, the temperature rises rapidly to $T \sim 10^4$ K. The subsequent collapse proceeds almost isothermally by efficient Lyman- α cooling. The cloud becomes optically thick to the ionization radiation when $n \sim 10^3 \text{ cm}^{-3}$, and the thermal evolution converges to that of the case without ionizing radiation. This is consistent with the 1D radiation hydrodynamics calculation of Kitayama et al. (2001).

Figure 21(b) shows the evolution with the QSO-type radiation. For comparison, the evolution with 10^2 and 10^3 times stronger X-ray intensities is also calculated. In the case with 10^3 times stronger X-ray intensity, DC does not occur. This case with a very strong X-ray intensity is an extreme example, and we do not expect that such conditions are realized in the early universe. Overall, neither ionizing radiation nor X-rays have a significant impact on the thermal evolution of the DC cloud of S1 (note a similar conclusion by Inayoshi & Tanaka 2015, for the former case).⁷

7.3. Effect of Metal Enrichment

Our model includes metal enrichment within progenitor halos, but we do not consider “external” metal enrichment by nearby halos. We have shown that the DC halos in our simulations approach very close (~ 100 pc) to the light source halos. The distance is well inside the virial radius of the source halo $\simeq 700$ pc, and thus the DC halos could be polluted by metals dispersed from the star-forming (light source) halo by, e.g., galactic winds.

We can estimate how far the metals will be dispersed around the star-forming halo as follows. The dynamics of an SN-driven bubble in the expanding universe is approximately described by the Sedov–Taylor-type self-similar solution (Voit 1996). The time evolution of the

position R of a shell around the bubble is described by

$$R = 23.6 \text{ ckpc} \left[\left(\frac{f_*}{0.005} \right) \left(\frac{f_b}{0.16} \right) \left(\frac{f_{\text{esc}}}{0.1} \right) \left(\frac{M_{\text{halo}}}{10^8 M_\odot} \right) \right]^{1/5} \left(\frac{21}{1+z} \frac{\hat{t}}{10^{10} \text{ yr}} \right)^{2/5} \left(\frac{\alpha}{0.5} \right), \quad (33)$$

where $d\hat{t} = (1+z)^2 dt$, t is the elapsed time after the SN explosion, and f_{esc} is the fraction of the energy injected into the wind to the total SN explosion energy. We have used the conversion efficiency between the SN explosion energy and stellar mass assuming the Salpeter IMF. The factor α represents uncertainty originating from effects such as the gravitational force from the host halo, external pressure, etc. More detailed numerical calculations suggest that this factor is around 0.5 (Barkana & Loeb 2001; Kitayama & Yoshida 2005), which is adopted in equation (33). Since the above size is smaller than or comparable to the virial radius of the light source halo, we only consider potential effects of the metal enrichment after the DC cloud plunges into the light source halo.

In our two cases S1 and S2, the density of the DC cloud reaches $\sim 100 \text{ cm}^{-3}$ when it passes through the virial radius of the light source halo. Cen & Riquelme (2008) point out that, once such a dense core is formed, metal mixing into the core takes a much longer time than the local dynamical time. Smith et al. (2015) also show that the densest part of a cloud collapses before it is significantly enriched with metals transported by mixing. It would be interesting to explore cases where the external metal enrichment from the light source halo prevents DC under peculiar conditions.

7.4. Observational Signatures of DC Halos

Recently, a strong helium-line-emitting galaxy without signatures of heavy elements has been discovered by Sobral et al. (2015). Several authors propose that the galaxy, called CR7, may be powered by an intermediate-mass BH hosted by a primordial halo as expected in the DC model (e.g., Pallottini et al. 2015; Agarwal et al. 2016; Hartwig et al. 2016). CR7 actually consists of three components: a helium line emitter without metals, and two small galaxies with spatial separations of $\simeq 5$ kpc. It is interesting, even encouraging, that our successful DC systems, with a DC halo and nearby light source halo(s), resemble the observed structure of CR7 (e.g., Pallottini et al. 2015).

For our S1 and S2, however, the separations between the DC and light source halos are much smaller than 5 kpc. Such small separations are a general feature of the DC candidate halos in our simulations. Also, the resulting short separations suggest strong tidal force that affects whether the main cloud collapses (Section 6). It will be interesting to examine whether the structure of CR7 is really realized in cosmological hydrodynamical simulations.

8. CONCLUSION

We have performed SPH/ N -body simulations to follow the evolution of gas clouds in early DM halos. We find two cases out of 42 samples, where the cloud collapses gravitationally and the gas condenses to densities of $\sim 10^8 \text{ cm}^{-3}$. The two cases are clear examples of DC

⁷ The temperature fluctuation that appeared in the one-zone calculation (Fig. 21) is caused by using the density evolution from the hydrodynamical simulation. The fluctuation amplitudes are so small that they do not affect the overall evolution of the temperature.

realized in the cosmological setup. The other 40 cases (halos) are identified as potential DC systems, but the clouds do not collapse because of the dynamical interaction between the host halo and the light source halo. In many cases, this is inevitable because strong LW radiation from a nearby massive halo is a necessary condition for the DC. Also, ram pressure stripping disturbs the cloud collapse moving in a dense environment.

In the two successful cases (S1, S2), we expect the gas cloud to yield a very massive star by mass accretion. The estimated accretion rates from the radial infall rates are $\dot{M} \sim 0.1 - 1 M_{\odot} \text{ yr}^{-1}$ for $M(< R) \lesssim 10^5 M_{\odot}$. Interestingly, the total mass of the infalling gas is reduced by an environmental effect. The outer part of the cloud core is subject to tidal disruption. Clearly, the tidal force exerted by nearby halos plays an important role, by disrupting the gas cloud itself in the failed cases, and by limiting the available gas mass for star formation in the successful cases.

We have also revisited the critical LW intensity required for the DC, considering the environmental effects included in our simulations. DC actually occurs even with 2% of the original LW intensity realized in our cosmological simulation. The critical intensity for DC should be determined at the density of $n_{\text{LTE}} \sim 10^3 \text{ cm}^{-3}$, not at the virialization of atomic-cooling halos as has been often assumed in previous studies. The LW intensity is highly variable in both time and space, and thus

it is necessary to follow the evolution of a DC system using three-dimensional simulations in order to determine robustly whether or not DC actually occurs.

Finally, we argue that the number density of the DC events is significantly smaller than the estimates in the previous studies. The expected number density of DC gas clouds, two in a cube of $20 h^{-1} \text{ Mpc}$ on a side, if we naively take our simulation result, is still larger than that of the observed high- z quasars. While the DC model provides a viable mechanism for the formation of ‘seed’ BHs, we still appear to be a long way from fully understanding the formation of SMBHs in the early universe.

ACKNOWLEDGEMENT

We thank K. Omukai, K. Sugimura, K. Inayoshi, G. Chiaki, Y. Sakurai, H. Susa, M. Umemura, J. Wise, M. Latif, T. Hartwig, M. Habouzit, and M. Volonteri for fruitful discussions and comments. This work was financially supported by Advanced Leading Graduate Course for Photon Science program and by the Grants-in-Aid for Basic Research by the Ministry of Education, Science and Culture of Japan (25800102, 15H00776: T.H., 25287050: N.Y.) and by Grant-in-Aid for JSPS Fellows (S.H.). The numerical simulations were carried out on XC30 at the Center for Computational Astrophysics (CfCA) of the National Astronomical Observatory of Japan. We use the SPH visualization tool SPLASH (Price 2007) in Figs 5, 7, 11, and 14.

REFERENCES

- Agarwal, B., Johnson, J. L., Zackrisson, E., et al. 2016, *MNRAS*, 460, 4003
- Agarwal, B., Khochfar, S., Johnson, J. L., et al. 2012, *MNRAS*, 425, 2854
- Barkana, R. 2004, *MNRAS*, 347, 59
- Barkana, R., & Loeb, A. 2001, *Phys. Rep.*, 349, 125
- Becerra, F., Greif, T. H., Springel, V., & Hernquist, L. E. 2015, *MNRAS*, 446, 2380
- Belczynski, K., Bulik, T., Fryer, C. L., et al. 2010, *ApJ*, 714, 1217
- Binney, J., & Tremaine, S. 1987, *Galactic dynamics* (Princeton, NJ, Princeton Univ. Press)
- Bond, J. R., Cole, S., Efstathiou, G., & Kaiser, N. 1991, *ApJ*, 379, 440
- Bromm, V., & Loeb, A. 2003, *ApJ*, 596, 34
- Bullock, J. S., Dekel, A., Kolatt, T. S., et al. 2001, *ApJ*, 555, 240
- Casares, J., & Jonker, P. G. 2014, *Space Sci. Rev.*, 183, 223
- Cen, R., & Riquelme, M. A. 2008, *ApJ*, 674, 644
- Choi, J.-H., Shlosman, I., & Begelman, M. C. 2015, *MNRAS*, 450, 4411
- Cole, S., Aragon-Salamanca, A., Frenk, C. S., Navarro, J. F., & Zepf, S. E. 1994, *MNRAS*, 271, 781
- Dekel, A., & Silk, J. 1986, *ApJ*, 303, 39
- Di Matteo, T., Khandai, N., DeGraf, C., et al. 2012, *ApJ*, 745, L29
- Dijkstra, M., Ferrara, A., & Mesinger, A. 2014, *MNRAS*, 442, 2036
- Dijkstra, M., Haiman, Z., Mesinger, A., & Wyithe, J. S. B. 2008, *MNRAS*, 391, 1961
- Gisler, G. R. 1976, *A&A*, 51, 137
- Glover, S. C. O., & Brand, P. W. J. L. 2003, *MNRAS*, 340, 210
- Grimm, H.-J., Gilfanov, M., & Sunyaev, R. 2003, *MNRAS*, 339, 793
- Gunn, J. E., & Gott, III, J. R. 1972, *ApJ*, 176, 1
- Habouzit, M., Volonteri, M., Latif, M., Dubois, Y., & Peirani, S. 2016, *MNRAS*, 463, 529
- Hahn, O., & Abel, T. 2013, *MUSIC: MULTI-Scale Initial Conditions*, Astrophysics Source Code Library, ascl:1311.011
- Hartwig, T., Latif, M. A., Magg, M., et al. 2016, *MNRAS*, 462, 2184
- Heger, A., & Woosley, S. E. 2002, *ApJ*, 567, 532
- Hirano, S., Hosokawa, T., Yoshida, N., Omukai, K., & Yorke, H. W. 2015, *MNRAS*, 448, 568
- Hirano, S., Hosokawa, T., Yoshida, N., et al. 2014, *ApJ*, 781, 60
- Hosokawa, T., Omukai, K., & Yorke, H. W. 2012, *ApJ*, 756, 93
- Hosokawa, T., Yorke, H. W., Inayoshi, K., Omukai, K., & Yoshida, N. 2013, *ApJ*, 778, 178
- Iliev, I. T., Mellema, G., Shapiro, P. R., & Pen, U.-L. 2007, *MNRAS*, 376, 534
- Iliev, I. T., Scannapieco, E., & Shapiro, P. R. 2005, *ApJ*, 624, 491
- Inayoshi, K., & Omukai, K. 2011, *MNRAS*, 416, 2748
- . 2012, *MNRAS*, 422, 2539
- Inayoshi, K., Omukai, K., & Tasker, E. 2014, *MNRAS*, 445, L109
- Inayoshi, K., & Tanaka, T. L. 2015, *MNRAS*, 450, 4350
- Inayoshi, K., Visbal, E., & Kashiyama, K. 2015, *MNRAS*, 453, 1692
- Inoue, A. K. 2011, *MNRAS*, 415, 2920
- Johnson, J. L., Dalla, V. C., & Khochfar, S. 2013, *MNRAS*, 428, 1857
- Kauffmann, G., White, S. D. M., & Guiderdoni, B. 1993, *MNRAS*, 264, 201
- Kitayama, T., Susa, H., Umemura, M., & Ikeuchi, S. 2001, *MNRAS*, 326, 1353
- Kitayama, T., & Yoshida, N. 2005, *ApJ*, 630, 675
- Kitsionas, S., & Whitworth, A. P. 2002, *MNRAS*, 330, 129
- Larson, R. B. 1969, *MNRAS*, 145, 271
- Latif, M. A., Bovino, S., Grassi, T., Schleicher, D. R. G., & Spaans, M. 2015, *MNRAS*, 446, 3163
- Latif, M. A., Bovino, S., Van Borm, C., et al. 2014, *MNRAS*, 443, 1979
- Latif, M. A., Schleicher, D. R. G., & Hartwig, T. 2016, *MNRAS*, 458, 233
- Latif, M. A., Schleicher, D. R. G., Schmidt, W., & Niemeyer, J. C. 2013, *MNRAS*, 436, 2989
- Leitherer, C., Schaerer, D., Goldader, J. D., et al. 1999, *ApJS*, 123, 3
- Loeb, A., & Furlanetto, S. R. 2013, *The First Galaxies in the Universe* (Princeton, NJ: Princeton Univ. Press)
- Luo, Y., Nagamine, K., & Shlosman, I. 2016, *MNRAS*, 459, 3217
- Machacek, M. E., Bryan, G. L., & Abel, T. 2001, *ApJ*, 548, 509

McCarthy, I. G., Frenk, C. S., Font, A. S., et al. 2008, MNRAS, 383, 593
 Milosavljević, M., Bromm, V., Couch, S. M., & Oh, S. P. 2009, ApJ, 698, 766
 Mo, H., van den Bosch, F. C., & White, S. 2010, Galaxy Formation and Evolution (Cambridge, UK: Cambridge University Press, 2010)
 Mortlock, D. J., Warren, S. J., Venemans, B. P., et al. 2011, Nature, 474, 616
 Omukai, K. 2001, ApJ, 546, 635
 Omukai, K., & Palla, F. 2003, ApJ, 589, 677
 O’Shea, B. W., & Norman, M. L. 2008, ApJ, 673, 14
 Pallottini, A., Ferrara, A., Pacucci, F., et al. 2015, MNRAS, 453, 2465
 Park, K., & Ricotti, M. 2011, ApJ, 739, 2
 Penston, M. V. 1969, MNRAS, 144, 425
 Planck Collaboration, Ade, P. A. R., Aghanim, N., et al. 2014, A&A, 571, A16
 Price, D. J. 2007, PASA, 24, 159
 Regan, J. A., Johansson, P. H., & Wise, J. H. 2014, ApJ, 795, 137
 Sakurai, Y., Hosokawa, T., Yoshida, N., & Yorke, H. W. 2015, MNRAS, 452, 755
 Sakurai, Y., Vorobyov, E. I., Hosokawa, T., et al. 2016, MNRAS, 459, 1137
 Schaerer, D. 2002, A&A, 382, 28
 Schleicher, D. R. G., Palla, F., Ferrara, A., Galli, D., & Latif, M. 2013, A&A, 558, A59
 Shang, C., Bryan, G. L., & Haiman, Z. 2010, MNRAS, 402, 1249
 Shlosman, I., Choi, J.-H., Begelman, M. C., & Nagamine, K. 2016, MNRAS, 456, 500
 Smith, B. D., Wise, J. H., O’Shea, B. W., Norman, M. L., & Khochfar, S. 2015, MNRAS, 452, 2822
 Sobral, D., Matthee, J., Darvish, B., et al. 2015, ApJ, 808, 139

Springel, V. 2005, MNRAS, 364, 1105
 Springel, V., White, S. D. M., Jenkins, A., et al. 2005, Nature, 435, 629
 Stecher, T. P., & Williams, D. A. 1967, ApJ, 149, L29
 Sugimura, K., Omukai, K., & Inoue, A. K. 2014, MNRAS, 445, 544
 Susa, H., Hasegawa, K., & Tominaga, N. 2014, ApJ, 792, 32
 Tanaka, T. L., Li, M., & Haiman, Z. 2013, MNRAS, 435, 3559
 Tegmark, M., Silk, J., Rees, M. J., et al. 1997, ApJ, 474, 1
 Toth, G., & Ostriker, J. P. 1992, ApJ, 389, 5
 Truelove, J. K., Klein, R. I., McKee, C. F., et al. 1997, ApJ, 489, L179
 Valiante, R., Schneider, R., Volonteri, M., & Omukai, K. 2016, MNRAS, 457, 3356
 Visbal, E., Haiman, Z., & Bryan, G. L. 2014a, MNRAS, 442, L100
 —. 2014b, MNRAS, 445, 1056
 Voit, G. M. 1996, ApJ, 465, 548
 Voit, G. M., Balogh, M. L., Bower, R. G., Lacey, C. G., & Bryan, G. L. 2003, ApJ, 593, 272
 Voit, G. M., Kay, S. T., & Bryan, G. L. 2005, MNRAS, 364, 909
 Volonteri, M. 2010, A&A Rev., 18, 279
 Wolcott-Green, J., & Haiman, Z. 2011, MNRAS, 412, 2603
 Wolcott-Green, J., Haiman, Z., & Bryan, G. L. 2011, MNRAS, 418, 838
 Wolfire, M. G., Hollenbach, D., McKee, C. F., Tielens, A. G. G. M., & Bakes, E. L. O. 1995, ApJ, 443, 152
 Wu, X.-B., Wang, F., Fan, X., et al. 2015, Nature, 518, 512
 Yoshida, N. 2006, New A Rev., 50, 19
 Yoshida, N., Abel, T., Hernquist, L., & Sugiyama, N. 2003, ApJ, 592, 645

- particles arranged in the order are grouped and combined with every N_{comb} particles.

APPENDIX

A. PARTICLE DE-REFINEMENT PRESCRIPTION

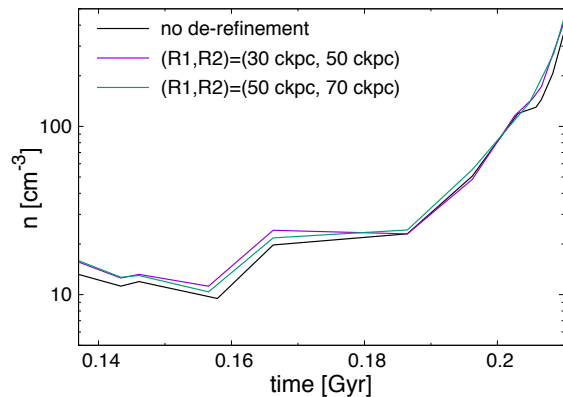


FIG. 22.— Effects of varying the particle de-refinement criteria for the density evolution for S1 halo. Each line shows the evolution without de-refinement (black) and with de-refinement using $(R_1, R_2) = (30 \text{ ckpc}, 50 \text{ ckpc})$ (purple) and $(R_1, R_2) = (50 \text{ ckpc}, 70 \text{ ckpc})$ (green).

To speed up the hydrodynamical calculation, we develop a de-refinement method that combines and subtracts gas particles in the simulation. We combine particles by the following steps:

- the region in which particles are combined is specified;
- the particles are sorted along the Peano–Hilbert curve; and

We combine every eight particles into one particle to de-refine them so that the energy and momentum are conserved. As control parameters, we set two distances from the center of the DC halo R_1 and R_2 , where $R_1 < R_2$. We carry out the de-refinement operation once for particles in $R_1 < R < R_2$ and twice for particles in $R_2 < R$, where R is the distance between the particle and the DC halo center.

We perform test calculations for the S1 halo, for which the de-refinement is done for the snapshot at $z = 24.6$, which corresponds to the cosmic age of 0.132 Gyr. Figure 22 shows the density evolution of the S1 halo with varying the de-refinement parameters R_1 and R_2 . The difference caused by the parameter choice is only within a factor of two. Nonetheless, the computation time with $(R_1, R_2) = (30 \text{ ckpc}, 50 \text{ ckpc})$ is smaller by an order of magnitude than that with $(R_1, R_2) = (50 \text{ ckpc}, 70 \text{ ckpc})$.

B. THE INFALLING VELOCITIES OF DC CANDIDATE HALOS

We derive the halo infalling velocity v_{inf} in the following steps: (1) we first assess the linear overdensity δ_{in} and the mass M_{in} within a distance d_{LW} , and (2) we calculate the turnaround radius R_{turn} of the mass shell at d_{LW} by the spherical collapse model. Here, the turnaround radius is defined by the radius at which the expansion of the mass shell turns to the contraction. The infalling velocity of the shell whose radius is R is defined as $v_{\text{inf}} = \sqrt{2GM(1/R - 1/R_{\text{turn}})}$, where $M = M(R)$ is the enclosed mass within R . The infalling time t_{inf} , the timescale over which the shell collapses from R_1 to R_2 ,

is

$$t_{\text{inf}} = \int_{R_2}^{R_1} \frac{dR}{v} = \int_{R_2}^{R_1} \frac{dR}{\sqrt{2GM(1/R - 1/R_{\text{turn}})}}. \quad (\text{B1})$$

In what follows, we derive M and R_{turn} as functions of R , which enables us to perform the above integration. Since we only consider the high- z universe at $z > 8$, which is the matter-dominant epoch, we assume the Einstein-de Sitter universe for simplicity below.

B.1. Linear Overdensity within R

The enclosed mass M and the linear overdensity δ within the shell radius R can be calculated by the spherical collapse model. Here, $\delta \equiv \rho/\bar{\rho} - 1$, where ρ is the density and $\bar{\rho}$ is the mean density of the universe, which is equal to $\Omega_m \rho_{\text{crit}}(1+z)^3$. In the Einstein-de Sitter universe, the dynamics of the shell $R = R(t)$ is parameterized by θ as follows:

$$\frac{R}{R_1(t)} = \frac{3}{10} \frac{1 - \cos \theta}{\delta(t)}, \quad (\text{B2})$$

$$\delta(t) = \frac{3}{5} \left[\frac{3}{4} (\theta - \sin \theta) \right]^{2/3}, \quad (\text{B3})$$

where $R_1(t) = [3M/(4\pi\bar{\rho}(t))]^{1/3}$. At the fixed t , two shells that have δ_i and θ_i , where $i = 1$ and 2 , have a relation as follows:

$$\frac{\delta_1}{\delta_2} = \left(\frac{\theta_1 - \sin \theta_1}{\theta_2 - \sin \theta_2} \right)^{2/3}. \quad (\text{B4})$$

The completely collapsed shell with $r = 0$ is characterized by $\theta = 2\pi$ and $\delta = \delta_c \equiv 1.69$. Assuming that the source halo has just reached $\theta_2 = 2\pi$ and corresponds to $\delta_2 = \delta_c$, then

$$\delta_1 = \delta_c \left(\frac{\theta_1 - \sin \theta_1}{2\pi} \right)^{2/3}. \quad (\text{B5})$$

With eqs. (B2) and (B5), the shell radius is determined by the enclosed mass and the linear overdensity as $R = R(M, \delta)$.

B.2. Enclosed Mass and Turnaround Radius

We evaluate the enclosed mass M within the shell radius R following Barkana (2004), which is based on the extended Press-Schechter (EPS) theory in the Fourier space (Bond et al. 1991) and the Press-Schechter (PS) theory in the real space. EPS theory can handle the contribution of the negative overdensity to the collapsed halo mass, while the negative overdensity never contributes in the PS theory and thus requires ad hoc treatment. In the EPS theory, it is convenient to evaluate the density field in the Fourier space. Instead of the wavenumber k , the variance $S_k \equiv 1/(2\pi^2) \int_0^k dk' k'^2 P(k')$ is used to represent the scale under consideration, where $P(k)$ is the power spectrum of the initial density fluctuation.

EPS theory provides the probability of the density lying between δ and $\delta + d\delta$, $Q(\nu, \delta, S_k) d\delta$, where ν is the critical overdensity for the collapsing halo. The cumulative mass function is obtained by integrating Q from ν to ∞ , while its differentiation gives the differential mass

function $f(\nu, S_k) dS_k$. Q and f can be written as follows:

$$Q(\nu, \delta, S_k) = \frac{1}{\sqrt{2\pi S_k}} \left[\exp\left(-\frac{\delta^2}{2S_k}\right) - \exp\left(-\frac{(2\nu - \delta)^2}{2S_k}\right) \right], \quad (\text{B6})$$

$$f(\nu, S_k) = \frac{\partial}{\partial S_k} \left[1 - \int_{-\infty}^{\nu} d\delta Q(\nu, \delta, S_k) \right] = \frac{\nu}{\sqrt{2\pi S_k^{3/2}}} \exp\left(-\frac{\nu^2}{2S_k}\right). \quad (\text{B7})$$

The probability distribution (δ, S_k) around $(\delta_c, S_{k,M})$ is given by

$$P(\delta|\delta_c) = Q(\delta_c, \delta, S_{k,M}) \frac{f(\delta_c - \delta, S_{k,M} - S_k)}{f(\delta_c, S_{k,M})}. \quad (\text{B8})$$

Therefore, the mean density profile $\langle \delta(r) \rangle$ around $(\delta_c, S_{k,M})$ becomes

$$\frac{\langle \delta(r) \rangle}{\delta_c} = 1 - \left(1 - \alpha + \frac{\alpha}{\beta} \right) \text{erf} \left[\sqrt{\frac{\beta(1-\alpha)}{2\alpha}} \right] - \sqrt{\frac{2\alpha(1-\alpha)}{\pi\beta}} \exp \left[-\frac{\beta(1-\alpha)}{2\alpha} \right], \quad (\text{B9})$$

where $\alpha \equiv S_k/S_{k,M}$ and $\beta \equiv \delta_c^2/S_{k,M}$.

It is pointed out by Barkana (2004) that in the rare halo limit where $\beta \sim 0$, the PS theory describes the density distribution more accurately than the EPS theory. In the PS theory, the mean density profile $\langle \delta(r) \rangle$ is given by

$$\frac{\langle \delta(r) \rangle}{\delta_c} = \frac{\xi_r(r_M, r)}{\sigma^2(r_M)}, \quad (\text{B10})$$

where ξ_r is the two-point correlation function. To compromise the EPS and PS theories, he adopts

$$\alpha = \frac{\xi_r}{\sigma^2(r_M)}, \quad \beta = \frac{\nu^2 \alpha (1 - \alpha)}{\sigma^2(r) - \alpha \xi_r(r_M, r)}, \quad (\text{B11})$$

instead of the values in the previous discussion.

Once the enclosed mass M is given, then we can derive the averaged density within the shell, $\delta = \delta(M)$ from eqs. (B9) and (B11). According to the discussion in Appendix B.1, the shell radius R and enclosed mass are related by $R = R(M, \delta(M))$. Therefore, for a given radius R , M , and δ within R are obtained by solving the equation $R = R(M, \delta(M))$.

With the obtained overdensity δ within the radius R , we can relate R and the turnaround radius R_{turn} corresponding to $\theta = \pi$ and $\delta = 1.06$ using eqs. (B2) and (B3) (Mo et al. 2010),

$$R_{\text{turn}} = \frac{2}{1 - \cos \theta_1} R, \quad (\text{B12})$$

where θ_1 is the parameter representing the considered shell given by eq. (B3). Inserting d_{LW} and d_{id} into R_1 and R_2 in eq. (B1), the infalling time is calculated for the given redshift z and source halo mass M_{source} .